Draft version December 11, 2012
Preprint typeset using LaTeX style emulateapj v. 12/16/11

GRB 120422A/SN 2012BZ - CONNECTING HIGH AND LOW-LUMINOSITY GRBS

S. Schulze[1,2,3]

Draft version December 11, 2012

ABSTRACT

Keywords: dust, extinction gamma rays: bursts : individual: GRB 120422A - supernovae: individual: SN 2012bz

1. INTRODUCTION

The discovery of the so-called hypernova SN 1998bw in the error-box of GRB 980425 by Galama et al. (1998) gave the study of the GRB-SN relation a flying start. This event remains bizarre in several ways among the many hundred GRBs that have been studied since. It is still the nearest GRB with a measured redshift and it is the intrinsically faintest GRB yet observed. Nevertheless, SN 1998bw seems to be well representative for the type of SN that accompany also more typical and brighter long-duration GRBs (for recent reviews see Woosley & Bloom 2006; Hjorth & Bloom 2011), i.e. a bright ($M = -19$ mag), broad-lined type Ic SN. Interestingly, in two cases no SN was found to deep limits to be associated with two nearby long-duration GRBs observed within a month of each other in 2006 (Fynbo et al. 2006; Della Valle et al. 2006a; Gal-Yam et al. 2006; Ofek et al. 2007; Kann et al. 2011), but since then no similar events have been observed.

So far, most GRBs with spectroscopically-confirmed SN associations have had a much lower apparent luminosity than the bulk of long-duration GRBs. GRB 030329 is the first and still the best example of a high-luminosity GRB that is accompanied by a SN (Hjorth et al. 2003; Matheson et al. 2003; Stanek et al. 2003), however there is a growing number of high-luminosity bursts with a spectroscopically-confirmed SN, such as GRBs 050525A (Della Valle et al. 2006b), 081007 (Della Valle et al. 2008), 101219B (Sparre et al. 2011), and 091127 (Berger et al. 2011). Bromberg et al. (2011) suggest that the low-luminosity GRBs are driven by high energy emission associated with shock break-out of the star, rather than an emerging jet as in typical high-luminosity GRBs. This may explain the different high energy emission properties of low luminosity GRBs.

The recent GRB 120422A is a particularly interesting case, with a luminosity intermediate between low and high luminosity GRBs and a robust detection of the associated SN (Malesani et al. 2012b; Sánchez-Ramírez et al. 2012; Wiersema et al. 2012; Melandri et al. 2012). A study of this object promises to answer important questions about the origin of both high and low luminosity GRBs. In this paper, we present our observations and findings of the transient following the GRB from mm to X-ray wavelengths, report on the spectroscopic properties of the accompanying GRB-SN, SN 2012bz, and the properties of the host galaxy and investigate its galaxy environment.

Throughout the paper we use the convention $F_\nu(t) \propto t^{-\alpha}\nu^{-\beta}$, where α is the temporal slope and β is the spectral slope. We adopt cm^{-2} as the linear unit of column densities, N. We assume a ΛCDM cosmology with $H_0 = 71\,\mathrm{km\,s^{-1}\,Mpc^{-1}}$, $\Omega_\mathrm{m} = 0.27$, and $\Omega_\Lambda = 0.73$ (Larson et al. 2011).

2. OBSERVATIONS AND DATA REDUCTION

On 22 April at 7:12 UTC (hereafter called T_0), the burst alert telescope (BAT, Barthelmy et al. 2005) aboard *Swift* detected and localised a faint burst (Troja et al. 2012). Its γ-ray light curve comprised a single peak with a duration of $T_{90} = 5.4 \pm 1.4$ s that is followed by a fainter and lower-energetic emission beginning 45 s after the trigger and lasting for 20 s. Within 86 s, the *Swift* X-ray telescope XRT (Burrows et al. 2005) and the UV/optical telescope UVOT (Roming et al. 2005) started to observe the field and detected an uncatalogued and rapidly decaying object at the UVOT-refined X-ray position $RA, DEC\,(\mathrm{J2000}) = 09^\mathrm{h}07^\mathrm{m}38.42^\mathrm{s}, +14°01'06.''0$ ($\pm 1.''8$, Goad et al. 2007; Evans et al. 2009). Cucchiara et al. (2012) detected a new source at $RA, DEC\,(\mathrm{J2000}) = 09^\mathrm{h}07^\mathrm{m}38^\mathrm{s}38, +14°01'07.''5$ ($\pm 0.''3$) inside the error box. Furthermore, they noted the proximity of a SDSS galaxy $2''$ NE of the explosion site (see also Tanvir et al. 2012). Spectra of the explosion site revealed a several absorption and emission lines at a common redshift of $z = 0.283$, and a plethora of emission lines at the location of the SDSS galaxy at the identical redshift of the GRB (Schulze et al. 2012a; Tanvir et al. 2012).

Since the redshift of GRB 120422A is in the range for which very stringent constraints on a possible accompanying GRB-SN can be placed and the fact that its γ-ray luminosity is between high and low-luminosity GRBs, we triggered an extensive imaging campaign with several telescopes from mm to optical wavelengths, as well as a large low- and medium-resolution spectroscopy campaign carried out at 6-m to 10-m class telescopes. These campaigns begun ~ 31 min after the trigger and were stopped ~ 44.6 days later. Furthermore, we obtained an X-ray spectrum with *XMM/Newton* 12 days after the explosion. In addition to our own efforts, the GRB-dedicated satellite *Swift* observed the GRB at UV/optical and X-ray wavelengths for 54.3 days. We incorporate these data as well to present a comprehensive study of this peculiar event. In the following we briefly summarise the observations and describe how these data were reduced. A log of our observations is shown in Tables 1, 2, and 8.

2.1. *Optical and NIR spectroscopy*

Our spectroscopic campaign begun 51 minutes after the trigger and covers a time span of 37.7 days. The

spectral sequence comprises seven medium-resolution spectra obtained with VLT/X-shooter and is complemented by five low-resolution spectra acquired with the Gemini Multi-Object Spectrograph (GMOS, Hook et al. 2004) mounted on Gemini-North, GTC/Osiris, the Keck Low Resolution Imaging Spectrometer (LRIS; Oke et al. 1995) and Magellan/LDSS3. A summary of our observation is shown in Table 1. Observing conditions were not always photometric because of bad weather or the moon distance (some spectra were obtained during full moon). For each epoch, we centred the slit on the explosion site and varied the position angle to probe different parts of the the host galaxy, as illustrated in Fig. 1. For the last X-shooter epoch, we set the position angle to the parallactic angle because of the high airmass. In the following we do not consider the X-shooter observation from 29 May due to poor weather conditions and high airmass.

VLT/X-shooter data were reduced with the X-shooter pipeline v1.4.10 (Goldoni et al. 2006) following Fynbo et al. (2010).[1] To extract the one-dimensional spectra of the transient and the host galaxy, we used an aperture of 1.″76–2.″24 for the UVB and VIS arms and an aperture of 2.″31–2.″94 for the NIR arm data. Gemini/GMOS-N and GMOS-S data were reduced with the dedicated `GMOS` spectroscopy package. We extracted the one-dimensional spectra within an aperture of **X.″X** with the `APALL` package in `IRAF`. The GTC and Magellan spectra were reduced and calibrated using standard procedures in `IRAF`. We had to take special care about the extraction of the spectrum obtained during the first GTC epoch due to the slit positioning. The one-dimensional spectrum of the first and second epoch were extracted within an aperture of 1.″25 and **X.″X**, respectively. Keck data were reduced with a custom pipeline that makes use of standard techniques of long-slit spectroscopy. To extract the one-dimensional spectrum, we chose an aperture of 1.″08 to minimise contamination from the host.

All spectra were flux-calibrated with the spectrophotometric standard stars shown in Table 1 and absolute flux-calibrated with our photometric data. The data were corrected for a Galactic reddening of $E(B-V) = 0.04$ mag (Schlegel et al. 1998). The wavelength calibration was done with respect to vacuum wavelengths. In addition, X-shooter data were corrected for barycentric and heliocentric motion. No attempt was made to correct for telluric absorption lines. This has no implications on our analysis.

TBD: Ruben: How big was the aperture during the 2nd epoch? GEMINI: aperture sizes

2.1.1. *Imaging*

Following the BAT trigger, *Swift* slewed immediately to the burst and UVOT took a v-band settling exposure 86 sec after the BAT trigger. Science observations began at $T_0 + 104$ s, starting with a 147 s *white* band (1600 − 6000 Å) exposure, a subsequent 246 s u-band exposure, after which observations cycled through the UVOT b ($\lambda_{\rm eff,\,b} = 4329$ Å), *white* ($\lambda_{\rm eff,\,wh} = 3470$ Å), $uvw2$ ($\lambda_{\rm eff,\,w2} = 2033$Å), v ($\lambda_{\rm eff,\,v} = 5402$ Å), $uvm2$ ($\lambda_{\rm eff,\,m2} = 2229$ Å), $uvw1$ ($\lambda_{\rm eff,\,w1} = 2591$ Å), u ($\lambda_{\rm eff,\,u} = 3501$ Å) filter sequence, initially with short 20 s exposures

[1] http://www.eso.org/sci/software/pipelines/

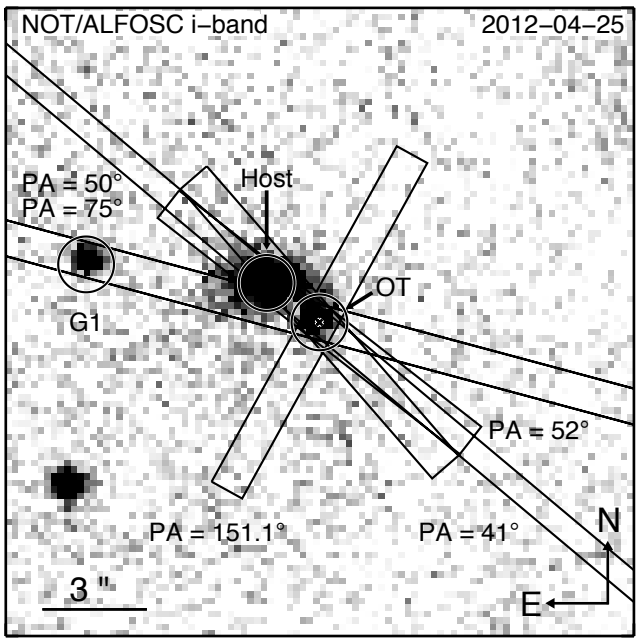

Figure 1. Field of view of GRB 120422A (18″ × 18″). The position of the optical transient, OT, accompanying GRB 120422A is marked, as well as the location of the putative host galaxy. Galaxy G1 is at $z_{\rm GRB}$. The transverse distance between the explosion site and the G1 is 28.7 kpc. The slit orientations of our spectroscopic campaign are superposed, see Table 1 for details.

that became progressively longer. Follow-up observations in the v and b band continued until $T_0 + 2.3$ days, in the $w1$, $m2$ and $w2$ UV filters they continued until $T_0 + 9.7$ days, and the GRB was observed in the u-band until $T_0 + 54.3$ days, at which time a final set of observations of the host galaxy were taken in all filters.[2]

We obtained the UVOT data from the *Swift* Data Archive.[3] These data have had bad pixels identified, mod-8 noise corrected, and have been transformed into FK5 coordinates. We used the standard UVOT data analysis software distributed with `HEASOFT 6.12` along with the standard calibration data. To minimise the contamination from the underlying host galaxy, the source flux was measured within a circular source extraction region with a 3.″5 radius. An aperture correction was then applied in order to remain compatible with the UVOT effective area calibrations, which are based on 5″ aperture photometry (Poole et al. 2008). The background was taken from a source-free region close to the source with a radius of 10″. The photometry was calibrated to the UVOT photometric system described in Poole et al. (2008).

Our ground-based imaging campaign begun 31 minutes after the explosion and spans a time interval of ∼ 45 days. The proximity of a $R = 8.24$ mag star (79″ NW of the explosion site) required special strategies to avoid excessive saturation. We either moved the optical transient to the NW corner of the chip, or (most of the time) obtained short dithered exposures.

[2] Additional UVOT data were acquired in October 2012. These data are not discussed in this paper. This has no implications on our work since the transient following the GRB was already fainter than the host galaxy at epoch $T_0 + 54.3$.

[3] http://www.swift.ac.uk/swift_portal/

Table 1
Summary of spectroscopic data

Phase	Telescope/Instrument	Arm/Grating	Spectral range (Å)	Resvoling power	Exposure time (s)	Slit width	Position angle	Standard star
Apr 22.3462 (+0.0449 days)	Gemini/GMOS-N	R400+OG515	6000–10000	959	2×900	1.″0	**XXX**	**XXX**
Apr 23.0167 (+0.7160 days)	VLT/X-shooter	UVB VIS NIR	3000-5500 5500–10000 10000–25000	4350 8800 5100	4×1200 4×1200 16×300	1.″0 0.″9 0.″9	41.°0	LTT3218
Apr 25.9114 (+3.6114 days)	GTC/Osiris	R500R	4800–10000	500	4×1500	**XXX**	75.°0	GD140
Apr 27.0140 (+4.7139 days)	VLT/X-shooter	UVB VIS NIR	3000-5500 5500–10000 10000–25000	4350 8800 5100	4×1200 4×1200 16×300	1.″0 0.″9 0.″9	41.°0	LTT3218
Apr 27.2566 (+4.95655 days)	Keck/LRIS	400/3400 400/8500	3000-5500 5500–10000		1800	0.″7	50.°0	Feige 34
May 1.0605 (+8.7604 days)	VLT/X-shooter	UVB VIS NIR	3000-5500 5500–10000 10000–25000	4350 8800 5100	4×1200 4×1200 16×300	1.″0 0.″9 0.″9	41.°0	GD153
May 6.**XXX** +14.6 days	GTC/Osiris	R500R	4800–10000	500	**XXX**	**XXX**	**XXX**	GD140
May 10.9963 (+18.6962 days)	VLT/X-shooter	UVB VIS NIR	3000-5500 5500–10000 10000–25000	4350 8800 5100	4×1200 4×1200 16×300	1.″0 0.″9 0.″9	52.°0	LTT3218
May 16.9993 (+24.6992 days)	VLT/X-shooter	UVB VIS NIR	3000-5500 5500–10000 10000–25000	4350 8800 5100	4×1200 4×1200 16×300	1.″0 0.″9 0.″9	52.°0	LTT3218
May 19.0681 (+26.7680 days)	Magellan/LDSS3	**XXX**	3700–9400	**XXX**	1×1400	**XXX**	141.°0	LTT4816
May 29.0251[a] (+36.7251 days)	VLT/X-shooter	UVB VIS NIR	3000–5500 5500–10000 10000–25000	4350 8800 5100	4×1200 4×1200 16×300	1.″0 0.″9 0.″9	-143.°9	GD153
May 30.0001 (+37.7001 days)	VLT/X-shooter	UVB VIS NIR	3000–5500 5500–10000 10000–25000	4350 8800 5100	4×1200 4×1200 16×300	1.″0 0.″9 0.″9	151.°1	GD153

Note. — Column "Phase" shows the logarithmic mean-time after the burst in the observer frame. Resolving powers were taken from the instrument manuals **Dan, Giulliano, Nino, and Rúben add missing information.**
[a]Observation was aborted due to bad weather. The total integration time is 4792 s.

Observations were carried out with the 2.2-m Nordic Optical Telescope (NOT) equipped with ALFOSC, MOSCA, and StanCAM in $u'g'Rr'Ii'$ bands (Malesani et al. 2012a; Schulze et al. 2012b). These observations begun at $T_0 + 0.5955$ day and were stopped at 44.5 days because of the small sun distance. Further imaging data were acquired with GMOS-N and GMOS-S in in $u'g'r'i'z'$ bands between 31 minutes and 40.7 days after the explosion (Cucchiara et al. 2012; Perley et al. 2012a). The Gamma-ray Optical/Near-infrared Detector (GROND, Greiner et al. 2007, 2008) mounted at the ESO/MPI 2.2 m telescope on La Silla imaged the field simultaneously in four optical ($g'r'i'z'$) and three NIR (JHK) bands starting at $T_0 + 16.5$ hr (Nardini et al. 2012). Additional epochs were obtained at nights 2, 9, 11, 20, 29 and were stopped at night 39 after the trigger, when the visibility of the field was compromised by its small sun-distance. We monitored the optical in $g'r'i'$ bands with the 60-inch Palomar telescope the for 37 days beginning at $T_0 + 0.87$ day and in JHK bands with Wide Field Camera (WFCAM) mounted at the United Kingdom Infrared Telescope (UKIRT) on Mauna Kea at seven epochs between $T_0 + 0.06$ and 25.98 day.

We complemented these optical observations with the 10.4-m GTC telescope equipped with OSIRIS in $g'r'i'z'$ bands, the multi-filter imager BUSCA mounted at the 2.2-m telescope of Calar Alto (CAHA) in g' and r' bands,[4], the 3.5-m CAHA telescope equipped with the Omega$_{2000}$ camera in z band,[5] the Low Dispersion Survey Spectrograph 3 (LDSS3) mounted at the 6-m Clay telescope telescope in r' and i' bands, the Direct CCD Camera mounted on the Irenee du Pont 2.5-m telescope at Las Campanas in r' and i' bands, and the 2.4-m Gao-Mei-Gu (GMG) telescope in **?** and **?**. Additional NIR data were acquired with the Omega$_{2000}$ in $YJHK_s$ bands, the Near-Infrared Imager (NIRI) mounted on Gemini-North in J and K-bands, and the Wide-field InfraRed Camera (WIRC) on the 200-inch Hale telescope at Palomar Observatory in J-band (Perley et al. 2012b).

Apart from these broad-band observations, we made use of the tuneable filters to observe the Hα emission of the host galaxy on 16 May, 25.5 days post burst. Ob-

[4] http://www.caha.es/newsletter/news01a/busca/
[5] http://www.mpia-hd.mpg.de/IRCAM/O2000/

servations consisted of 5×600 s exposures using a 15-Å filter tuned to the wavelength of Hα at the redshift of the burst ($\lambda_{\rm obs}$ = 8420Å), and a 3 × 100 s exposure with a 513-Å-wide order-sorter filter centred at 8020 Å to probe the continuum emission (filter f802/51). The seeing was $\sim 1''$, but the transparency was affected by extinction due to Saharan dust suspended in the atmosphere.

Observing conditions were not always photometric; in particular, part of the NOT observations suffered under poor transparency due by Saharan dust in the atmosphere (Calima). In Table 8 we summarise all observations with good data quality.

The reduction of the NOT data was carried out following standard procedures. Short, dithered exposures were usually adopted to minimize the effects of to the bright star. Some observations suffered from variable conditions, and in those cases individual images were weighted according to their S/N. The *i*- and *z*-band images suffer from some fringing, which was corrected using a fringe pattern computed from the science data themselves, although in some cases the presence of the halo from the nearby bright star hampered the process. These data result in a lower S/N. Optical GMOS data (Gemini North and South) were bias-subtracted and flat-fielded using the `GEMINI/GMOS` package in `IRAF`.[6] Images were then aligned and coadded using the `imcoadd` package to obtain a final stack in each filter. Gemini/`NIRI` data were reduced with a dedicated reduction package to construct a coadded frame in the two filters. Bad pixels as well as fringing correction were performed by the dedicated tools. GROND optical/NIR image reduction and analysis was performed in standard fashion using a custom pipeline with `IRAF/pyraf` (Tody 1993) tasks. For details on the GROND data processing we refer to Yoldaş et al. (2008) and Krühler et al. (2008). UKIRT data was reduced with the dedicated reduction pipeline.[7] P200/WIRC data were reduced using a modified version of `WIRCSoft` that is based on standard IR reduction techniques.[8] Other optical and NIR data were were processed through standard procedures (bias subtraction, flat field normalisation) using `IRAF`.

Astrometric calibration was computed against the USNO-B1 catalog (Monet et al. 2003), yielding an RMS of 0.″4. All images were then registered together, yielding a relative RMS of less than 0.″08.

TBD: CAFOS: Javier, Dong: Add missing information

2.1.2. *Submm/mm observations*

Our mm/submm observations comprise five epochs and cover a time interval of 9.48 days. First, Smith et al. (2012) obtained an early epoch at 850 μm with the submillimeter continuum camera SCUBA-2 on the James Clerk Maxwell Telescope (JCMT). The 1.5 hours lasting observation begun at $T_0+ \approx 41$ min and was performed under moderate weather conditions. In the consecutive night, Martin et al. (2012) triggered a short 45 min snapshot observation at the Submillimeter Array (SMA) at $T_0 + 21.4$ hr. Receivers were tuned to the local oscillator (LO) centre frequency of 271.8 GHz ($\lambda = 1.1\,\mu$m), with the correlator configured to cover two 4 GHz bands centred at ±6 GHz from the LO frequency. All 8 SMA antennas were used in its very extended configuration under excellent weather conditions, with an average zenith opacity of 0.03 (perceptible water vapour (PWV) $\sim$ 0.5 mm) at 225 GHz. A further observation was carried out by Perley (2012) with the Combined Array for Research in Millimeter-Wave Astronomy (CARMA) in the D-configuration at 92.5 GHz ($\lambda = 3$ mm). This observation was carried out between 23:13 UT on 24 April and 00:29 UT on April 25 and the total on-source integration time was 58 minutes. We finally obtained two epochs with the Plateau de Bure Interferometer (PdBI) at a frequency of 86.7 GHz ($\lambda = 3.4$ mm) in its 6 antenna compact D configuration . These observations begun at $T_0 + 2.6416$ and 9.5048 days and lasted for 84 min each.

Table 2
Log of mm and submm observations

Phase (days)	Instrument	Frequency	Exposure time (s)	F_ν (mJy)
0.0285	SCUBA-2	353 GHz	5400	< 8.40
0.8917	SMA	272 GHz	3420	< 3.60
2.6416	PdBI	86.7 GHz	5040	< 0.39
2.6937	CARMA	92.5 GHz	3480	< 1.15
9.5048	PdBI	86.7 GHz	5040	< 0.24

Note. — Column "Phase" shows the logarithmic mean-time after the burst in the observer frame. Upper limits are measured at the 3σ confidence level.

We reduced CARMA and SMA data with the `MIRIAD` and `MIR-IDL` software packages (Sault et al. 1995).[9][10] CARMA data were absolute flux-calibrated with observations of 3C84 and Mars. The calibration of the SMA data is twofold; first we we used the nearby quasars J0854+201 and J0909+013 as atmospheric gain calibrators, and then J0854+201 for bandpass calibration. Absolute flux calibration was bootstrapped from previous measurements of these quasars resulting in an absolute flux uncertainty of $\sim$ 30%. PdBI data were reduced with the standard `CLIC` and `MAPPING` software distributed by the Grenoble GILDAS group.[11] The flux-calibration was secured with the Be binary star system MWC349 ($F_\nu(86.7\,{\rm GHz}) = 1.1$ Jy).

TBC: SCUBA-2: How was the data reduced?

2.1.3. *X-ray observation*

Swift/XRT started to observe the BAT GRB error circle 86.3 seconds after the trigger while it was still slewing. As aforementioned *Swift* detected a new rapidly decaying source that was observed for 80 s in `windowed-timing` mode. After that the count rate was $\ll 1\,{\rm cts\,s^{-1}}$ XRT switched to `photon-counting` mode. Observations continued until $T_0+53.8$ days, when the visibility of the field was compromised by its small sun-distance. We obtained the temporal and spectroscopic data from the *Swift*/XRT Light curve and Spectrum Repository (Evans et al. 2007, 2009).

To analyse the spectroscopic data we used `Xspec` version 12.7.1 as part of `HeaSoft` 6.12 and the calibration files version 13. The X-ray emission till $T_0 + 200$ s are in

[6] http://iraf.noao.edu/
[7] http://casu.ast.cam.ac.uk/surveys-projects/wfcam
[8] http://humu.ipac.caltech.edu/~jason/sci/wircsoft/index.html
[9] http://www.atnf.csiro.au/computing/software/miriad/
[10] https://www.cfa.harvard.edu/~cqi/mircook.html
[11] http://www.iram.fr/IRAMFR/GILDAS

detail discussed in Starling et al. (2012) and Zhang et al. (2012). Therefore, we focus on the analysis of the data after that epoch. In total XRT registered 270 background-subtracted photons from the GRB that were not flagged as bad and are at energies > 0.3 keV after $T_0 + 200$ s. Owing to the low number of counts, we re-binned the spectrum to have at least 1 count per bin and applied Cash statistics. Data were fitted with an absorbed power law, where the Galactic absorption component was fixed to $N_{\rm H,\,gal} = 0.371 \times 10^{21}$ cm^{-2} (Kalberla et al. 2005) and the second component was left free to account for host absorption. As absorption model we choose `phabs`.

TBD: XMM: Andrew

2.2. *Photometry*

Measuring the brightness of the transient is complicated by the blended host galaxy. To limit the host contribution to the transient photometry, we used point-spread function (PSF) fitting techniques. Using bright field stars, a generic model of the PSF was constructed and fitted to the optical transient. To provide reliable fit results, all images were registered astrometrically to a precision of better than 0.″08, and the centroid of the fitted PSF was held fixed with a small margin of recentering corresponding to the uncertainty of the astrometrical alignment of the individual images. Also the PSF-fitting radius was adjusted to the specific conditions of the observations and instrument, in particular seeing and pixel scale. The fit radius is different for each observations, but typically in the range between 0.″5 and 0.″8. Generally, the radius was smaller under unfavourable sky conditions in the attempt to minimise the host's effect on the fit. Naturally, this leads to a smaller signal-to-noise ratio for these measurements than one would expect for isolated point sources.

For images taken under adverse sky conditions (seeing $\gtrsim 1.''6$), with imagers of large pixel scales (e.g. the NIR channels of GROND with 0.″6 per pixel), or in filters/epochs with low S/N (e.g. most of the late NIR data), the individual contributions of point-source and galaxy can not be disentangled robustly. These measurements are ignored in the following.

To measure the brightness of the transient in the UVOT images, we measured the host galaxy flux at the position of the SN from our later UVOT observations, where there was no longer a contribution from the GRB or SN. This additional flux was then subtracted from our photometric measurements at the position of the GRB. For all observations the source was close to the centre of the field of view, and differences in the PSF between observations were, therefore, negligible.

In contrast, host-galaxy photometry was performed via standard apertures. Here, we used our PSF-model to subtract the transient from the deepest images in each filter with the clearest separation between galaxy and point source, i.e. those images with the smallest FWHM of the stellar PSF. A circular aperture radius was chosen sufficiently large (2.″5, e.g. 10.6 kpc at $z = 0.2825$), so that the missed emission from low surface brightness regions does not affect our photometry significantly. In addition we also corroborated the galaxy photometry using elliptical Kron apertures (Kron 1980) via their implementation in `Source Extractor` (Bertin & Arnouts 1996).

Once a magnitude was established, it was calibrated photometrically against the brightness of a number of field stars measured in similar manner. Photometry was tied to the SDSS DR8 (Aihara et al. 2011) in the optical filters ($u'g'r'i'z'$) and 2MASS (Skrutskie et al. 2006) in the NIR (JHK_S). For those filter bands not covered by our primary calibration systems (e.g. $I_{\rm C}$ or Y) we used the instrument-specific band passes to transform magnitudes into the respective filter system via synthetic photometry similar to the procedure outlined in Krühler et al. (2011a).

The photometric error is then estimated based on the contributions from photon statistics and goodness of the PSF fit (typically between 0.5 to 15 %), the absolute accuracy of the primary calibration system ($\approx 2-3\%$), the systematic scatter of different instrument/bandpasses with respect to the primary calibrators ($\approx 3-6\%$) or the uncertainty in the colour transformation (if applicable, $\approx 6-9\%$).

Despite all efforts, any contribution of host flux directly underlying the transient can not be accurately resolved, and does miss from the galaxy magnitudes or contributes to our measured transient photometry. We thus caution, that, strictly speaking, our measurements represent transient brightness plus underlying host emission. The latter contribution, however, is expected to be smaller than 0.1 mag at early times or SN peak when the transient is bright. This estimate is based on archival SDSS images.

The data were corrected for a Galactic reddening of $E(B-V) = 0.04$ (Schlegel et al. 1998). This corresponds to extinctions in the UVOT filters of $A_v = 0.11, A_b = 0.15, A_u = 0.17, A_{w1} = 0.24, A_{m2} = 0.34$ and $A_{w2} = 0.32$ mag.

2.3. *Spectral energy distribution fitting*

The spectral energy distribution (SED) of the GRB host galaxy was modelled with `Le Phare` (Arnouts et al. 1999; Ilbert et al. 2006).[12] We used a grid of galaxy templates based on Bruzual & Charlot (2003) stellar population-synthesis models with the Chabrier initial mass function (IMF; Chabrier et al. 2000) and a Calzetti dust attenuation curve (Calzetti et al. 2000). For a description of the galaxy templates, physical parameters of the galaxy fitting and their error estimation we refer to Krühler et al. (2011b). To account for zeropoint offsets in the cross calibration and absolute flux scale, an systematic error contribution of 0.05 mag was added in quadrature to the uncertainty introduced by photon noise.

3. RESULTS

3.1. *The transient accompanying GRB 120422A*

Figure 2 displays the brightness evolution of the transient accompanying GRB 120422A at UV, optical and NIR wavelengths. During the first three days, the brightness in the UVOT filters gradually decreases with a decay slope of $\alpha = 0.2$ that is followed by a rebrightening peaking at ~ 20 days post-burst. The time scale and the colour evolution of the rebrightening are comparable to those of GRB-SNe (e.g. Zeh et al. 2004). The initially decaying transient could therefore be a superposition of the afterglow (originating from the shocks between the

[12] http://www.cfht.hawaii.edu/~arnouts/LEPHARE

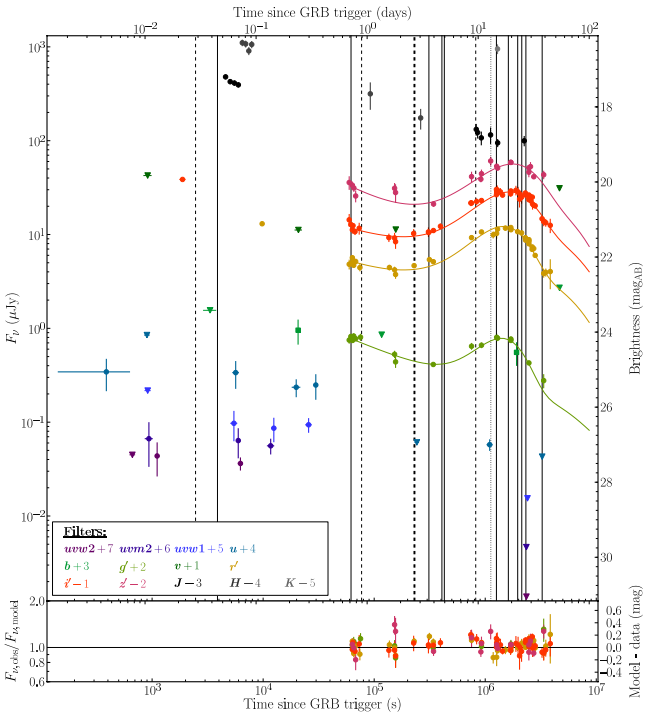

Figure 2. Multi-band light curve of the optical transient following GRB 120422A. Triangles indicate 3σ upper limits. Data are not corrected for host extinction. UVOT v-band upper limits are very shallow and are not displayed in that figure. Vertical lines indicate the mid-exposure times of the optical spectra (solid lines) summarised in Table 1 and displayed in Fig. 4, the submm/mm observations summarised in Tab. 2 and the XMM observation (dotted line) at **XXX** days. Data in $g'r'i'z'$-bands were modelled with a SN 1998bw template at $z = 0.283$ imposed on power law using the formalism in Zeh et al. (2004); the model parameters are shown in Sect. 3.2.3. Fit residuals are displayed in the bottom panel.

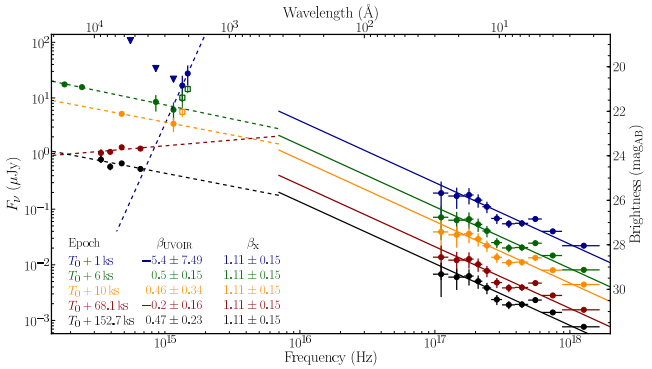

Figure 3. Spectral energy distribution from NIR to X-ray energies at 1, 6, 10, 68.1, 152.7 ks. Upper limits are indicated by triangles. SEDs were fitted with a simple power law $F_\nu \propto \nu^{-\beta}$. (The displayed X-ray data is already corrected for Galactic and host absorption.) The best fit of the UV/optical/NIR and X-ray (UVOIR) SED is displayed in dashed and solid lines for each epoch, respectively. Data points disregarded during the fit are not filled.

GRB jet and the circumburst medium) and the cooling phase that follows the shock-break out from the supernova.

To discern between these models, we built NIR-to-X-ray SEDs between 1 and 152.7 ks after the burst. These are shown in Fig. 3. The X-ray emission can be described by a simple power law $F_\nu \propto \nu^{-\beta}$ (after being corrected for Galactic and host extinction). The value of the spectral slope and its lack of evolution are characteristic for GRB X-ray afterglows at these epochs. The NIR-to-UV emission appear to consist of two distinct radiation components. The blue colour of the UV emission, despite the large errors, is rather characteristic for the cooling of the shock break-out (e.g. Ensman & Burrows 1992; Campana et al. 2006, and references therein). This has been observed in a number of Ib/c SNe, such as 1993J (Blinnikov et al. 1998), 1999ex (Stritzinger et al. 2002), 2006aj Campana et al. (2006), 2008D (Modjaz et al. 2009), and 2011dh (Soderberg et al. 2012). These cases have in common that the shock break-out is strongest in the bluer bands and gradually disappears at longer wavelengths, e.g. the dip was less than 0.2 mag in V and reached almost 1 mag in the U band in SN 2008D. In the case of GRB 120422A, the dip in the i'-band is about 0.4 mag, with respect to the first detection (this prominent feature is at 6000 Å in the rest frame), while it is ~ 2.3 mag in the u-band. This is comparable to the shock break-out of GRB 060218 (Campana et al. 2006). These authors reported a rise in brightness till 0.57 days post burst (shifted to the observer frame of GRB 120422A). However, the brightness of GRB 120422A only decreases since the earliest observation at 86.4 seconds after the explosion.

The NIR-to-UV SED at $T_0 > +6$ ks can be fitted with a simple power law that has a slope similar to $\beta_x - 1/2$. The value and the observed flux-density level agree with an afterglow model where the cooling frequency is in between the optical and X-ray bands. We caution that the SED at $T_0 + 68.1$ ks is not consistent with being afterglow emission making the interpretation of the SED at 152.7 ks as originating from the afterglow component doubtful. However, the fact that the slope and the observed flux-density ratio at the last epoch point to the same afterglow model, provides circumstantial evidence for the interpretation.

In the following section we will present the findings on the SN and in Sect. 3.3.

3.2. *Supernova properties*

3.2.1. *Supernova Spectrum*

Our spectra of SN 2012bz are presented in Fig. 4. The very early spectra are dominated by a smooth power-law continuum, characteristic of GRB afterglows. At around 4.7 days, after the transient started re-brightening (Fig. 2), the shape of the spectrum changes and it becomes redder. By 1 May (8.8 days after the GRB), the spectrum has clearly started to resemble that of a supernova with broad lines (Malesani et al. 2012b; Sánchez-Ramírez et al. 2012; Wiersema et al. 2012, see also Fig. 5). By May 10, the transformation is complete and our X-shooter spectra from +18.7 and +24.7 days are very similar to those of other SNe Ic-BL, accompanying GRBs (Fig. 5). The Magellan spectrum from May 19 is of low S/N and despite that it shows absorption troughs at locations consistent with the previous data, it should be interpreted with great caution.

Figure 5 shows the comparison of SN 2012bz at two different phases with simultaneous spectra of SNe 1998bw,

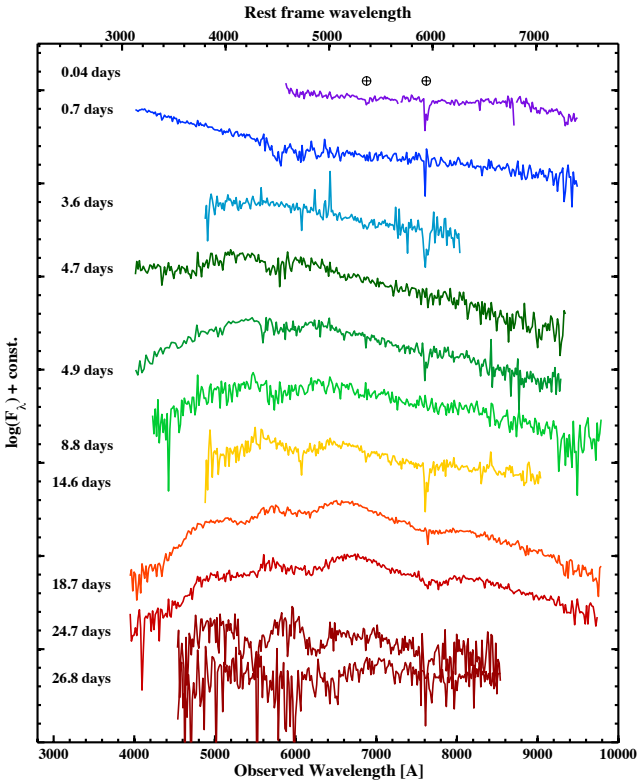

Figure 4. Spectral evolution of the optical transient accompanying GRB 120422A. The spectra have been shifted by an arbitrary constant and are displayed chronologically with respect to the GRB time All spectra have been binned to increase S/N and for presentation purposes. Depending on the telescope, the binning applied results to a resolution of 15-20 Å. The location of prominent telluric lines is marked with the Earth symbol.

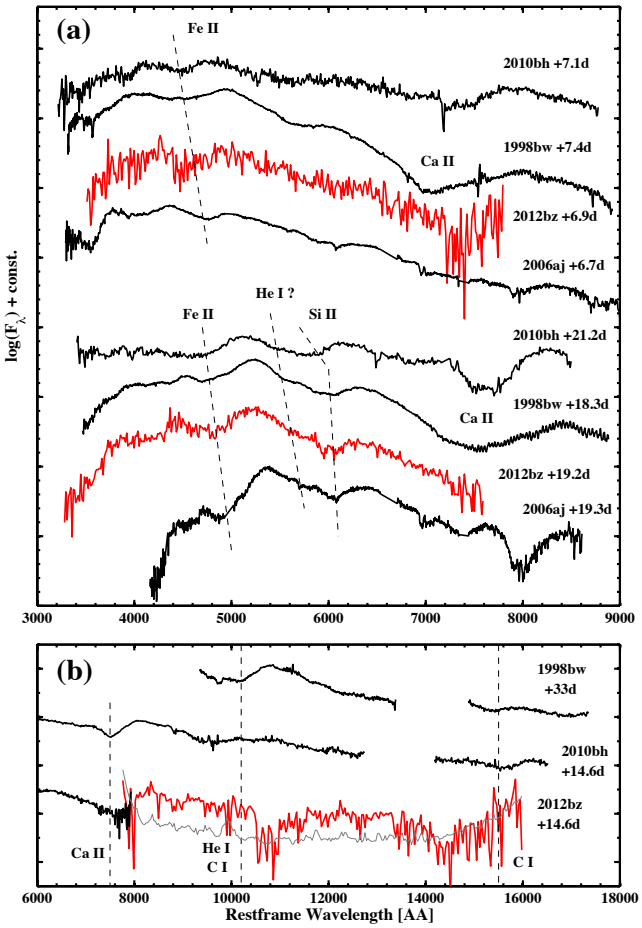

Figure 5. (a) Comparison of SN 2012bz (red) to that of other GRB-SNe (black) at two different phases, ~ 7 and ~ 20 days past explosion, respectively. All comparisons are made in the rest frame. The dashed lines connect the approximate minima for the Fe II and Si II features and the spectra are shown in an expansion velocity sequence from the fastest (SN 2010bh) to the slowest (SN 2006aj). A less significant (but real) feature that has been proposed to be He I is also identified. (b) NIR arm of the X-shooter spectrum of SN 2012bz at maximum light (red). The thin grey line is the error spectrum. The Ca II IR triplet at the redshift of SN 2012bz is located between the VIS and NIR arms. For comparison NIR spectra of SN 1998bw and SN 2010bh are shown along with identification of the most prominent lines (Patat et al. 2001; Bufano et al. 2012). Unfortunately these features fall in unfavourable atmospheric regions of our spectrum. It is not clear if the flux suppression between 10500–11000 Å (rest frame) is due to real SN absorption feature or if it is instrumental.

2006aj and 2010bh (Patat et al. 2001; Pian et al. 2006; Bufano et al. 2012). Overall, the spectra are very similar and show the same features, although line strengths and expansion velocities vary from object to object. In Fig. 5, we have illustrated this by annotating the main features as they have been identified in the past (e.g. Patat et al. 2001): Fe II, usually visible between 4500–5000 Å; Si II, around 5600–6100 Å; the Ca II IR triplet (that for SN 2012bz is in a noisy part of the spectrum between the VIS and the NIR arms; see lower panel); and possibly He I, at around 5500 Å (e.g. Bufano et al. 2012). We stress that these SNe have very large explosion velocities and that their broad-lines are likely the result of blending, making line identification not straightforward. Nevertheless, all SNe displayed in Fig. 5 are remarkably similar, reinforcing the idea that the nature of these blends, whatever it is, is the same for all GRB-SNe, pointing towards similar explosions. Differences do however exist in the expansion velocities and the spectra have been displayed in an 'expansion velocity sequence' going from the 'fastest' (SN 2010bh; see also discussion in Chornock et al. 2010; Bufano et al. 2012) to the 'slowest' (SN 2006aj). This is at least true for the Fe II and Si II lines and, in that respect, SN 2012bz seems intermediate and more similar to SN 1998bw. For SN 2012bz, the Si II line is contaminated by the telluric A-band making velocity measurements difficult and, for this reason, below, we present a comparison of the explosion velocities of GRB-SNe based on the Fe II line. The Ca IR triplet shows a different velocity behaviour, not correlated with the one determined by the other elements, and SN 1998bw is clearly faster at all phases.

It is interesting to point out that the nitch that has been possibly identified as He I is also visible in SN 2012bz, and as a matter of fact in most optical GRB-SNe spectra with sufficient S/N to the left of the main Si II trough. A powerful diagnostic to test the presence of He I is NIR spectroscopy (Patat et al. 2001; Bufano et al. 2012). Our X-shooter NIR spectra are unfortunately of low S/N and for this reason we focus our analysis only on the one obtained at maximum light (Fig. 5; lower panel). Still, however, this spectrum is

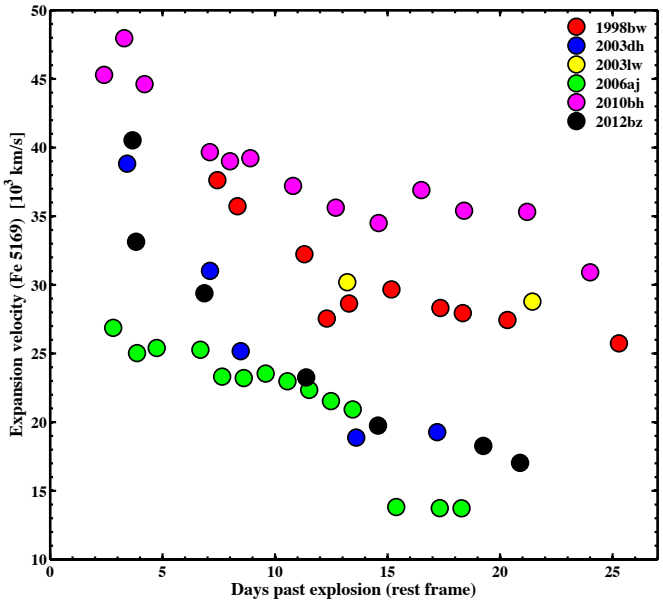

Figure 6. Expansion velocities measured from Fe IIλ5169 for SN 2012bz and the other five GRB-SNe with very good spectroscopic data. Measurements were performed on our data as well on the spectra of Patat et al. (2001), Hjorth et al. (2003), Malesani et al. (2004), Pian et al. (2006) and Bufano et al. (2012). They assume that the feature measured is Fe IIλ5169. **Giorgos, could you write the ion as Fe IIλ5169?**

dominated by a weak continuum, while all prominent features are located in an unfavourable region (the error spectrum is displayed). For comparison, we have also plotted an X-shooter spectrum of SN 2010bh obtained at a similar phase (Bufano et al. 2012). SN 1998bw does not have a contemporaneous spectrum but we show the one obtained at $T_0 + 33$ day, where the identified features are more clearly visible (Patat et al. 2001). Both the locations where one would expect to see He Iλ10830 or C Iλ10695 and C Iλ16890 are located in very noisy atmospheric regions of our spectra, at the redshift of SN 2012bz, preventing us from drawing any meaningful conclusion. There is a possible flux suppression between 10500–11000 Å (rest frame) where the continuum is lost but it is not easy to identify this with any SN feature (and besides its significance is low). Usually, GRB-SN explosion velocities are reported with respect to the Si II line, with the Ca II line reported sometimes as the only alternative (Patat et al. 2001; Hjorth et al. 2003; Chornock et al. 2010; Bufano et al. 2012). Pian et al. (2006) shows expansion velocities that have been derived from model spectra fits. In the case of SN 2012bz, the Si II line is contaminated by the telluric A-band, while the Ca IR triplet is redshifted outside the optical spectrum. For this reason we chose to measure the expansion velocities based on the Fe II feature. In addition, this feature appears earlier than the Si II feature and its minimum is easier to locate as it lies between two well visible maxima (Fig. 4, 5). This makes it a potentially better expansion velocity tracer for GRB-SNe, than Si II that, especially at early times, is super-imposed on a blue continuum and it is not always easy to locate and measure. We have used the fiducial rest-wavelength of 5169 Å for Fe II, as done e.g. in Hamuy & Pinto (2002) for the expansion velocities of SNe IIP. We stress that even if this identification is not correct for GRB-SNe, due to blending, these measurements are still valuable in order to monitor the expansion velocity evolution and for comparison between different objects as long as the measurements are done consistently. Based on these assumptions, we present the first, to our knowledge, diagram of GRB-SNe expansion velocities, based on Fe IIλ5169 (Fig. 6). Our conclusions are that: (i) the velocities measured for these features are reasonable (of the order of 25–45000 km/s and decelerating with a reasonable rate), thus confirming that this is a useful expansion velocity indicator, (ii) SN 2010bh shows again the fastest explosion velocities, while SN 2006aj the slowest (Chornock et al. 2010; Bufano et al. 2012), (iii) SN 2012bz shows large velocities at 3 days past explosion (the earliest spectrum where a measurement is possible) and slowing down to 15000 km/s at around 20 days later. This behavior is very similar to SN 2003dh.

3.2.2. *The bolometric light curve*

The knowledge of the evolution of the expansion velocity allowed us to construct the bolometric light curve of the GRB-SN. An estimate of the bolometric light curve was initially constructed using $g'r'i'z'$ photometric points, as coverage outside these bands is limited around the SN peak. The light curves in each filter were fitted with spline interpolations starting at 2 days past the GRB trigger, such that an estimated magnitude for all four bands was available at each epoch of observation. Magnitudes were converted into monochromatic fluxes at the effective (rest-frame) wavelengths of the filters for every epoch to produce an SED.[13] Each SED was then integrated over the limits of the filter wavelength range (3000-8000 Å), assuming zero flux at the blue edge of g' and the red edge of z' bands. The integrated fluxes were converted to luminosities using the redshift and cosmology of the paper. The resulting light curve (Fig. 7) gives a luminosity of the SN over approximately the optical wavelength range.

Contributions to the flux outside this regime, however, are not insignificant. This is particularly true in the NIR, wherein the fraction of the total luminosity emitted increases with time, reaching a comparable contribution to the optical within 30 days (e.g. Valenti et al. 2008). By using the fractional NIR flux of a similar transient, an estimate of the missing flux can be applied to SN 2012bz. A photometric study by Olivares E. et al. (2012) of the low redshift ($z = 0.059$) XRF100316D/SN 2010bh contains well sampled light curves in $z'JH$ bands, extending upon our rest-frame wavelength limits. The contribution of wavelengths > 8000 Å to the flux was determined by first integrating SN 2010bh's dereddened SED over the same wavelength range used for SN 2012bz above, and then over the wavelength range redward of 8000 Å. Thus, for each epoch of observation, we obtain the NIR contribution as a fraction of the optical flux. The phase of the contributions were normalised so $t = 0$ was the peak of the respective SNe, and stretched by a factor $\Delta m_{15(3000-8000)\,\text{Å}}$ to match the light curve shape of the

[13] Since we are evaluating the SED for every observation, nearby epochs (within < 0.2 day of each other) were first calculated individually and then averaged when producing the final light curve for clarity.

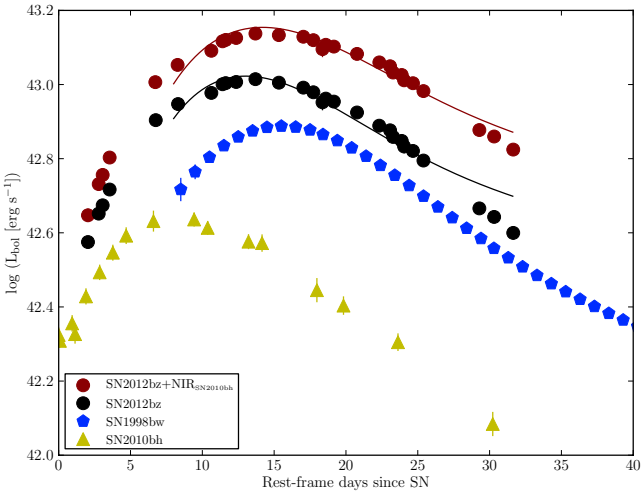

Figure 7. Pseudo-bolometric light curves of SN 2012bz from direct integration of the SED over $g'r'i'z'$ filters, and including a NIR contribution as found for SN 2010bh. For comparison the $UBVRI$ light curve of SN 1998bw (Clocchiatti et al. 2011) and the $g'r'i'z'JH$ lightcurve of SN 2010bh are shown (Olivares E. et al. 2012). The models for SN 2012bz are shown as solid lines. Early light-curve time data are not fitted as the anaytical model does not account for other non-negligable sources of luminosity at these times (see text). Only photometric and calibration uncertainties are included in the error bars.

two SNe (0.78 for SN 2012bz, 1.00 for SN 2010bh).[14] The fractional values were interpolated using a smooth spline, in order to sample it at the epochs of SN 2012bz observations, and the appropriate amount was added to the optical flux. This gives a NIR corrected light curve covering 3000–17000 Å. No attempt was made to account for flux missed below 3000 Å, due to the paucity of data constraining the UV in such objects.

The bolometric light curve of a stripped-envelope SNe can be modelled using the simplified analytical prescription of Arnett (1982), updated by (Valenti et al. 2008) to obtain physical parameters of the explosion, the mass of ^{56}Ni, the mass ejected and the kinetic explosion energy ($M_{\rm Ni}$, $M_{\rm ej}$ and $E_{\rm K}$ respectively). Since obtaining a truly bolometric light curve is unfeasible, we use our optical and optical+NIR correction light curves as good approximations. Our data cover the photospheric phase of SN evolution, when the ejecta are considered optically thick. The opacity is chosen to be $\kappa = 0.07$ cm^2 g^{-1} (see Cano et al. 2011). To constrain the $E_{\rm K}/M_{\rm ej}$ ratio, a *scale velocity* is required (see equation 54 in Arnett 1982), this is taken to be the photospheric velocity ($v_{\rm ph}$) at peak. Fe II lines are a good tracer of $v_{\rm ph}$ (Valenti et al. 2011), and the peak of the pseudo-bolometric light curve occurs at ∼13.9 days (from fitting low-order polynomials around peak). Using data in Fig. 6 we take 20500 km s^{-1} as an estimate of $v_{\rm ph}$ at peak by linearly interpolating between the measurements taken from spectra at epochs 11.380 days and 14.575 days.

Fitting to the optical bolometric light curve reveals the following parameters: $M_{\rm Ni} = 0.40 \pm 0.01\ M_\odot$, $M_{\rm ej} = 4.72 \pm 0.04\ M_\odot$ and $E_{\rm K} = 3.29 \pm 0.03 \times 10^{52}$ erg, when including the NIR contribution from SN 2010bh, we obtain $M_{\rm Ni} = 0.58 \pm 0.01\ M_\odot$, $M_{\rm ej} = 5.87 \pm 0.03\ M_\odot$ and $E_{\rm K} = 4.10 \pm 0.03 \times 10^{52}$ erg. The first 8 days were ignored in the fit as contribution from other sources (GRB afterglow, SN shock-breakout) would compromise the assumptions of the SN model. SN 2012bz shows one of the highest nickel masses ever seen in a GRB-SNe (Bufano et al. 2012).

It is crucial to note the errors quoted here include only the statistical uncertainties relating to the construction of the pseudo-bolometric light curves. Systematic errors arise from both the simplifying assumptions in the model (spherical symmetry, centrally concentrated ^{56}Ni mass etc.) and our choice of parameters for the fit, these typically dominate statistical errors. For example taking an uncertainty in $v_{\rm ph}$ of 2000 km s^{-1} translates to an error in $M_{\rm ej}$ and $E_{\rm K}$ of ∼ 10% and ∼ 25% respectively. The two-component model for hypernovae by Maeda et al. (2003) would also suggest we are only observing the outer, lower density region of the ejecta during the photospheric phase ($\lesssim$ 30 days), and a fraction is hidden in a denser, inner component during this time. Although the afterglow component is not expected to contribute significantly around the SN peak (**quantify, is the afterglow modelled?**), potential contamination by underlying host galaxy light is included in this bolometric light curve (Sect. 2.2).

Melandri et al. (2012) modelled SN 2012bz using a scaled spectral model for SN 2003dh to obtain estimates of the physical parameters. They obtained values of $M_{\rm Ni} \approx 0.35\ M_\odot$, $M_{\rm ej} \approx 7\ M_\odot$ and $E_{\rm K} \approx 3.5 \times 10^{52}$ erg using a bolometric light curve covering 3300–7400 Å. Comparing these to our values for the optical (3000–8000 Å) bolometric light curve, the $M_{\rm Ni}$ values are in good agreement, given our slightly extended wavelength range, $E_{\rm K}$ values are consistent, however we underestimate the ejected mass compared to their value. Differences could be caused by choices of $v_{\rm ph}$ and κ, or asymmetries, which spectral modelling can account for.

One thing to note is the importance of the NIR contribution to the extracted parameters from such modelling. We observe a ∼ 45% increase in the nickel mass obtained, and a ∼ 25% increase in $M_{\rm ej}$ and $E_{\rm K}$. Although SN 2010bh was clearly different from SN 2012bz, the NIR contribution as a fraction of the optical is not expected to be wildly varying across SN of the same type. The contribution of the NIR is clear when comparing the analytical models to the data in Fig. 7; we find much better agreement at late times when including a NIR correction, when the fractional flux contained at these longer wavelengths is substantial.

3.2.3. *SN 2012bz in the k, s paradigm*

The first systematic study of the "late red bumps" in the light curves of GRB afterglows was performed by Zeh et al. (2004). They used the multi-color light curves of the prototypical GRB-SN 1998bw (Galama et al. 1998; Patat et al. 2001) as template light curves. They derived the SN 1998bw light curves at the given GRB redshift, and in the given observed band (hereby including the cosmological k-correction), and additionally modified the template with two parameters. The luminosity factor k determines the peak SN luminosity in a given band in units of the SN 1998bw peak luminosity in that

[14] Phillips (1993) introduced Δm_{15} as the decline in the brightness between the SN maximum and 15 days later in a given band.

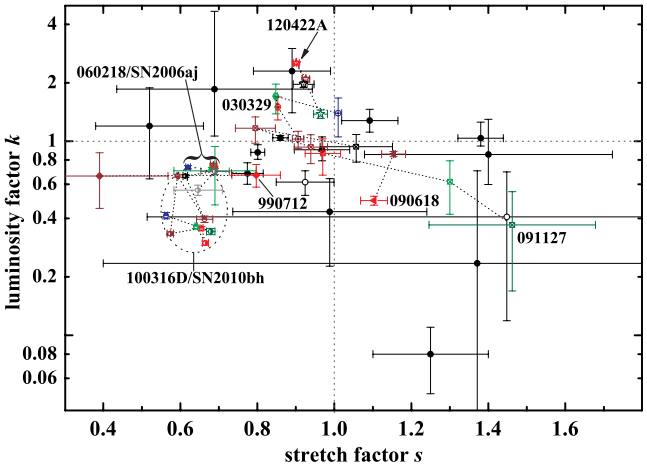

Figure 8. Comparison of GRB-SNe. We plot the luminosity factor k (peak luminosity in units of the SN 1998bw peak luminosity) vs. the stretch factor s (time dilation vs. the SN 1998bw light curve), see text for more details. Black circles are R_C-band data (observer frame). GRB-SNe where multi-color light curves could be fitted are color-coded (e.g. green = V/g', red = R_C/r', etc.), and values in different bands of a single SN are connected by dotted lines (going from bluer to redder bands). We find that SN 2012bz associated with GRB 120422A (dotted stars) evolves slightly slower than SN 1998bw, but is significantly more luminous, up to a magnitude ($k \approx 2.5$) in r'. This makes it one of the most luminous GRB-SNe known.

band. The stretch factor s determines if the light curve evolution is faster ($s < 1$) or slower ($s > 1$) than that of SN 1998bw, hereby, the actual evolutionary shape remains the same, and the explosion time is always identical to the GRB trigger time.

Ferrero et al. (2006) studied SN 2006aj, associated with XRF 060218 (Campana et al. 2006; Pian et al. 2006), in comparison to an increased sample of GRB-SNe as well as other stripped-envelope SNe (Richardson et al. 2006) in the k, s paradigm. This sample has been further enlarged in Thöne et al. (2011).We fit our $g'r'i'z'$ data set following the method of Zeh et al. (2004), fitting the early data with a component following a power-law decay, wherewith we allow the decay slope to be different in each band, similar to the approach Ferrero et al. (2006) used with SN 2006aj. The results of our fits are given in Table 3 and reveal the SN 2012bz is significantly more luminous than SN 1998bw, by up to a whole magnitude in r'. The evolution is slightly faster than that of SN 1998bw, and it is somewhat redder, with g' being the relatively least luminous band. This makes SN 2012bz one of the most luminous GRB-SNe detected so far.

The SN-fit makes several assumptions. We assume no host galaxy extinction (Table 3.3), any additional extinction would make the SN more luminous. Similarly, if the power-law component were to break to a steeper slope after a few days, the actual SN contribution would also be more luminous. On the other hand, any contribution of a host galaxy underlying the SN light (which we assumed to be negligible) will dim the SN luminosity. The host galaxy influence can only be estimated from late images, taken once the SN fades away.

3.3. *The afterglow emission*

We detect no source in the final maps of our submm/mm observations at the position of the optical and X-ray transient. Table 2 summarises the 3σ flux-density limits. From observations and theory, it is known that the peak flux density of the afterglow synchrotron spectrum is expected to cross the submm/mm bands between ~ 1 day and several days after the burst. Hence, our observations probed this time interval, we use these limits as a proxy of the peak luminosity of the afterglow emission.

Table 3
Properties of the SN modelling

Band	Decay slope α	k	s	χ^2/d.o.f.
g'	0.49 ± 0.04	1.38 ± 0.07	0.96 ± 0.02	12.8/14
r'	0.57 ± 0.02	2.53 ± 0.04	0.90 ± 0.01	73.2/35
i'	0.46 ± 0.06	2.09 ± 0.05	0.93 ± 0.01	43.8/36
z'	0.69 ± 0.12	1.96 ± 0.07	0.92 ± 0.03	22.6/16

Note. — Best-fit parameters of the $g'r'i'z'$ band light curve fits. We modelled light curves with a SN1998bw template redshifted to $z = 0.2825$, as described in Zeh et al. (2004), superposed on a power law ($F \propto t^{-\alpha}$) to to account for the early emission.

Figure 9 shows the limits on the peak flux density of GRB 120422A and of other GRBs. The observations with the PdBI are among the deepest ever reported for a GRB in the pre-ALMA era. All limits on 120422A point to a very small peak luminosity density of $< 10^{31}\,\mathrm{erg\,s^{-1}\,Hz^{-1}}$ and possibly even less than $10^{30}\,\mathrm{erg\,s^{-1}\,Hz^{-1}}$. These limits are exceptionally deep for high-luminosity GRBs, e.g. the afterglow of GRB 030329, a burst with spectroscopically confirmed SN and $E_{\rm iso} > 10^{51}$ erg, had a peak luminosity density that is at $\sim$ 100-times larger; and the afterglow of GRB 080319B, a burst with photometric evidence for a SN, was about $\sim$ 10-times more luminous. Intriguingly, the peak luminosity density is in the expected range of low-luminosity GRBs, such as GRB 060218. This is consistent with the very weak detection at radio wavelengths (Zauderer et al. 2012).

We should try to construct an SED from mm to X-ray energies.

3.4. *Environments*

3.4.1. *Explosion site*

The X-shooter spectrum, obtained on April 23.0167, exhibits few absorption lines. We detect weak Mg II and Ca II, but no Mg I or Na I in absorption (see Table 4). After applying the heliocentric correction, we obtain an absorption redshift of $z_{\rm abs} = 0.28253 \pm 0.00003$, refining the redshift measurements by Schulze et al. (2012a) and Tanvir et al. (2012).

The Mg II doublet consists of two velocity components that are separated by $150\,\mathrm{km\,s^{-1}}$. Ca II absorption is only found in the blue velocity component of the Mg II doublet. The line ratio of the latter of 2.07 ± 0.06 is consistent with the theoretical one of 2.0, but almost twice as large as the average observed line ratio of 1.16 ± 0.03 derived from an GRB afterglow composite spectrum presented by Christensen et al. (2011). Because the observed and expected line ratio of the Mg II doublet are consistent, we infer a total Mg II column density (both velocity components) of $(5.65 \pm 0.24) \times 10^{13}\,\mathrm{cm^{-2}}$ in the weak-line limit.

The derived column density is smaller compared to that of the majority of GRBs, but there are cases

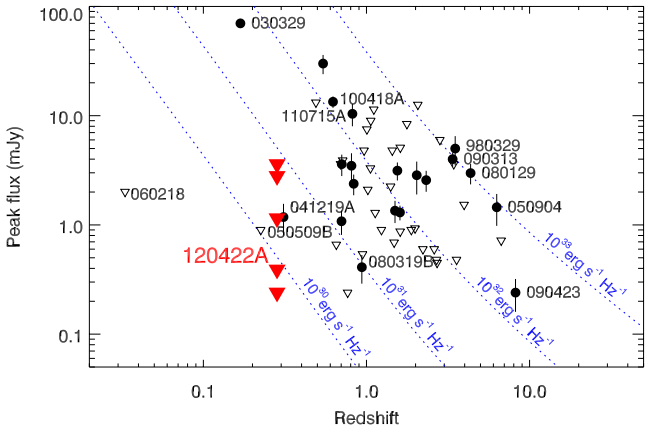

Figure 9. Peak flux density measured in mm/submm wavelengths vs. redshift. Triangles indicate 3σ detection limits. The limits on the peak flux density of GRB 120422A are shown in red. Dotted lines display flux density levels for equal luminosity at varying redshifts. Some interesting bursts are indicated in the figure, e.g. GRB 030329 is a cosmological burst with a spectroscopically-confirmed SN, GRB 080319B is the naked-eye burst with a photometrically-confirmed SN, GRB 060218 is a low-luminosity GRB with spectroscopically-confirmed SN, and GRB 050509B is a short burst, i.e. a burst that originated from the coalescence of a binary system of compact objects. Figure adapted from de Ugarte Postigo et al. (2012). **Antonio: Could you colour-code GRBs with spectroscopically-confirmed SN, GRBs with photometrically-confirmed SN, low-luminosity and short bursts? Could you label GRBs with spectroscopically-confirmed SN?**

with comparable or smaller column densities, e.g. GRBs 050922C (Piranomonte et al. 2008) and 070125 (De Cia et al. 2011). The non-detection of Mg I is indicative for a tenuous environment. Such environments are rare. This finding is very intriguing because the detection of the accompanying GRB-SN unambiguously points to a massive star origin (Malesani et al. 2012b; Wiersema et al. 2012). Such an environment has been observed before. The most nearby burst GRB 980425 ($z = 0.0085$, Tinney et al. 1998), the rosetta stone event that revealed the connection between GRBs and the death of massive stars, occurred in the outskirts of its host galaxy. Based on deep *HST* images, Fynbo et al. (2000) also showed that the stellar cluster, of which the progenitor of GRB 980425 was part, is either very small or very faint, pointing towards a tenuous environment.

TBC: Johan, Martin, Steve; Question: In which environments are low-luminosity GRBs found?

3.4.2. *Host Galaxy*

Figure 1 displays a zoom-in on the GRB position at 3.5849 days after the explosion. A curved bridge of emission connecting the transient with the host is clearly visible. This suggests that the GRB occurred either in a spiral arm (however no counter arm is visible on the far side of the galaxy), or within an interacting companion.

Figure 10 shows a part of the two-dimensional spectrum obtained with X-shooter on 22 April. The radial profiles of the [O II] and Hα emission lines extend from the galaxy nucleus to explosion site. Their profile is not disturbed indicating that we see the galaxy face-on. The emission lines are strongest in the centre of the galaxy and gradually become weaker at larger galactocentric distances. Because both lines are proxies

Table 4
Absorption and emission lines at the explosion and the host site

$\lambda_{\rm obs}$ (Å)	Transition	redshift	$EW_{\rm obs}$ (Å)	$F \times 10^{16}$ (erg cm^{-2}s^{-1})
Explosion site				
	Mg II λ2796		3.10 ± 0.15	···
	Mg II λ2803		1.50 ± 0.17	···
	Mg I λ2852		$X.xx \pm Y.yy$	···
	Ca II λ3968		$X.xx \pm Y.yy$	···
	Ca II λ3933		$X.xx \pm Y.yy$	···
	Na I λ5891		$X.xx \pm Y.yy$	···
	Na I λ5897		$X.xx \pm Y.yy$	···
4780.29	[O II] λ3727	0.28258	···	0.15 ± 0.01
4783.78	[O II] λ3729	0.28255	···	0.23 ± 0.01
6423.89	[O III] λ4959	0.28266	···	0.23 ± 0.03
6564.61	Hα	0.28269	···	0.39 ± 0.02
Bridge (PA = 41°)				
Host site (PA = 41°)				
4780.21	[O II] λ3727	0.28256	···	2.42 ± 0.04
4783.74	[O II] λ3729	0.28255	···	3.51 ± 0.04
4920.66	Hη	0.28260	···	0.12 ± 0.01
4963.17	[Ne III] λ3869	0.28257	···	0.25 ± 0.03
4989.16	Hζ	0.28251	···	0.27 ± 0.02
5093.00	Hϵ	0.28249	···	0.14 ± 0.04
5262.13	Hδ	0.28253	···	0.30 ± 0.03
5568.35	H$\gamma^{\dagger}$	0.28253	···	1.15 ± 0.06
6236.94	Hβ	0.28261	···	1.33 ± 0.05
6362.08	[O III] λ5007	0.28260	···	0.80 ± 0.06
6423.62	[O III] λ4959	0.28261	···	2.48 ± 0.05
8419.82	Hα	0.28261	···	4.97 ± 0.10
8446.14	[N II] λ6583	0.28259	···	0.75 ± 0.03
8616.84	[S II] λ6717	0.28259	···	0.84 ± 0.04
8635.55	[S II] λ6731	0.28263	···	0.67 ± 0.03
Host site (PA = 75°)				
6240.33	Hβ	0.28331	···	0.98
6365.80	[O III] λ5007	0.28335	···	0.87
6426.86	[O III] λ4959	0.28326	···	2.17
8423.09	Hα	0.28311	···	4.61
8451.72	[N II] λ6583	0.28344	···	0.53
8620.83	[S II] λ6717	0.28318	···	0.94
8640.65	[S II] λ6731	0.28338	···	0.71

Note. — The reported observed wavelengths were corrected for heliocentric motion and were derived from measuring the first momentum of the line profile. The fluxes were corrected for foreground extinction. † the line is blended. The host spectrum at PA = 75° was not absolute flux-calibrated.

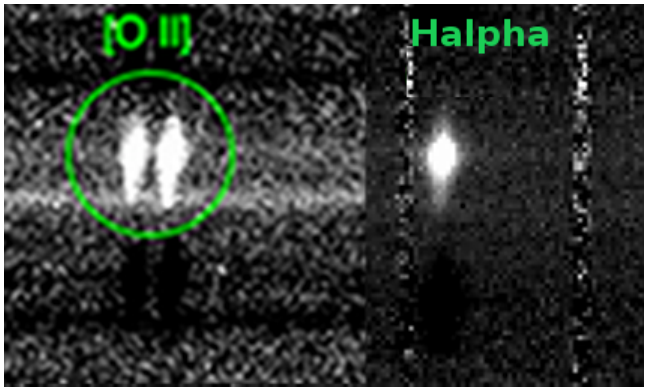

Figure 10. Part of the two-dimensional spectrum obtained with VLT/X-shooter on April 23.0167 (Table 1). The upper trace is the putative host galaxy and the lower the spectrum of the explosion site. **Dummy figure**

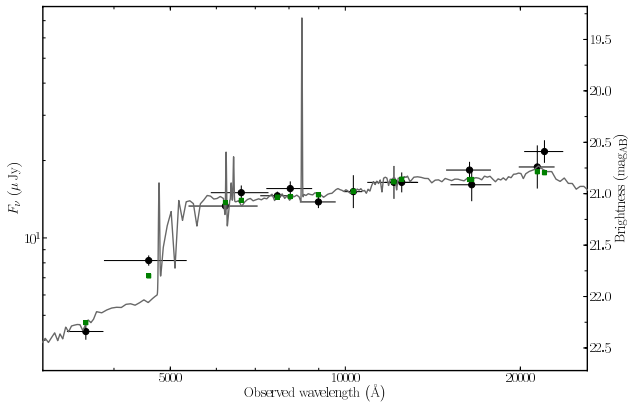

Figure 11. Spectral energy distribution of the GRB host galaxy from 350 to 2146 nm. The solid line displays the best fit model of the SED with `Le Phare` ($\chi^2 = X.X$; number of filters = 10). The green points are the model predicted magnitudes. **Thomas: What is the χ^2 value?**

for star formation and the extinction is similar in both lines of sight, the highest star-formation activity is not found at the explosion site, but in the centre of the host galaxy, see also the right panel in Fig. 12. In addition, the curved bridge is also a region of ongoing star formation. This result is puzzling because the detection of the GRB-SN unambiguously pointed to a massive star origin. Therefore, we expected the GRB to have occurred in a region of high/highest star formation as found by Fruchter et al. (2006). These authors also reported that the majority GRB host galaxies at $z < 1$ are irregular and only a few of them are grand-design spiral galaxies, such as GRB 990705. The distance from the explosion site to the nucleus of ~ 7.8 kpc is about six times larger than the median of Bloom et al. (2002) and the largest in their sample but not unheard of, e.g. the offsets of GRBs 011121 and 060505 are 9 and 11 kpc, respectively Greiner et al. (2003); Thöne et al. (2008).

Figure 11 display the observed host SED and its best fit; the best-fit values are summarised in Table 6. The observed SED is best described by a moderately massive, barely-extinguished and low-UV-luminous galaxy that has a low star-formation rate but a very young starburst. The comparison with the Savaglio et al. (2009) shows that the galaxy is not very different from normal host galaxies; it only stands out with respect to its low age of the starburst and the low star-formation rate.

In conclusion, the morphology and the burst location in the galaxy differs from most GRB hosts, however, the properties of the host are quite typical for GRB hosts.

Steve: Add results and discussion on metal lines, add metallicity measurement. What about low-luminosity hosts?

3.4.3. *GRB host galaxy environment*

In the previous section we briefly mentioned the possibility that the true GRB host is a satellite of the galaxy that is 7.82 kpc NE of it. Because we did not detect an enhanced star-formation activity at the explosion, could the GRB be a result of very localised star-formation activity triggered by galaxy interaction instead of being a natural product of an isolated star-forming region? To address this issue, we studied the nature of other objects close to the GRB position to find evidence for a galaxy overdensity or galaxy interaction. Our GTC spectrum from April 25.9114 revealed that object G1 is at the same redshift as the GRB. The transverse distance of 7.″1 corresponds to a proper distance of 28.7 kpc at $z = 0.283$. However, this strategy is very inefficient to search for star-forming galaxies in a larger area. The tuneable filters ($FWHM = 15$Å) at the GTC are a better solution. They enabled us to search for star-forming galaxies in area with a radius of a few hundred kpc in one shot. The side effect of this technique is that we can study the star-formation activity within the putative host galaxy. The SN is not contributing a lot to the continuum at this wavelength, so that we see the pure Hα emission in the host galaxy after removing the continuum. Figure 12 displays the i'-band image obtained with NOT/ALFOSC on April 26, the continuum image and Hα image.

We detect four galaxies that have emission consistent with Hα at z=0.283 (Fig. 12). We identify the closest one, located at 7.8 kpc of the GRB as the host. The galaxy G1 (23 kpc from the centre of the host galaxy), already identified with the GTC spectrum from April 25.9114, could be a satellite galaxy in interaction with the host, whereas G3 and G4 could be members of the same galaxy group. If this galaxy density is increased with respect to the field galaxy density at

Table 5
Brightness of the putative GRB host galaxy at optical/NIR wavelengths

Filter	$\lambda_{\rm center}$ (nm)	Brightness (mag)
u	357.88	22.34 ± 0.08
g	458.98	21.65 ± 0.05
r	621.96	21.12 ± 0.04
R	662.30	20.99 ± 0.07
i	764.01	21.02 ± 0.05
I	804.08	20.95 ± 0.07
z	898.93	21.08 ± 0.06
$J_{\rm UKIRT}$	1250.24	20.89 ± 0.10
$H_{\rm UKIRT}$	1635.35	20.77 ± 0.08
$K_{\rm UKIRT}$	2200.45	20.59 ± 0.11
$Y_{\rm CAHA}$	1032.28	20.98 ± 0.16
$J_{\rm CAHA}$	1212.41	20.89 ± 0.16
$H_{\rm CAHA}$	1649.59	20.91 ± 0.16
$K_{\rm CAHA}$	2138.97	20.74 ± 0.21

Note. — Magnitudes are given in the AB photometric system and are corrected for Galactic extinction. The brightness was measured within a circular aperture (diameter 2.″5). The brightness was measured in $u'RI$ with NOT, in $g'r'i'z'$ with GROND, in $YJHK$ with CAHA, and in JHK with UKIRT.

Table 6
Properties of the host galaxy

Parameter	Value	Median of Savaglio et al. (2009) sample $z < 0.5$ / all redshifts
M_B (mag)	-19.4 ± 0.1	$-19.4/-20.6$
M_K (mag)	-19.5 ± 0.2	$-20.0/-20.5$
A_V (mag)	$0.01^{+0.09}_{-0.01}$	...
$\log M_\star(M_\odot)$	8.95 ± 0.04	9.35/9.32
Age (Myr)	360^{+30}_{-40}	1220/1221
$SFR(M_\odot\,{\rm yr}^{-1})$	$0.3^{+0.4}_{-0.1}$	1.4/2.3

Note. — Magnitudes are given in the AB photometric system. The star-formation rate was measured from the UV continuum. The age represents the age of the starburst. The stellar mass was calculated assuming the Chabrier IMF (Chabrier et al. 2000). For comparison we show the median of each quality from the Savaglio et al. (2009) sample.

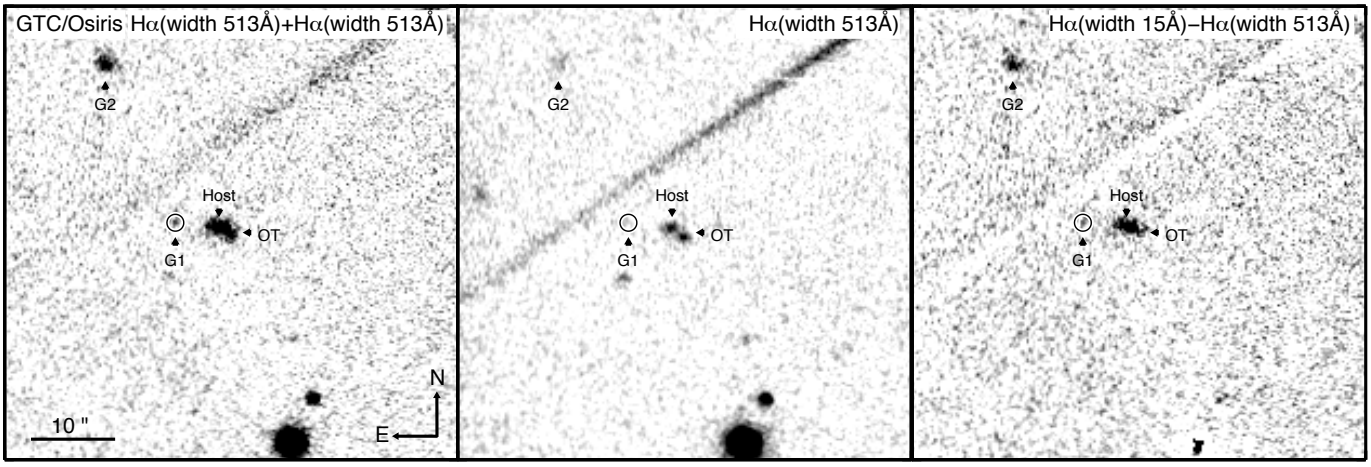

Figure 12. Galaxy environment of GRB 120422A. The field of view is centred on the the optical transient, OT, and has a size of 55.″2 × 55.″2. The left panel shows the i'-band image obtained with the 2.0-m NOT telescope on April 26 (brightness of the optical transient: $i' = 22.23\,\mathrm{mag_{AB}}$; Table 8). To identify star-forming galaxies at the redshift of the GRB, we observed the field with a narrowband ($FWHM = 513$Å) and a tuneable filter (width 15 Å) at the GTC centred at Hα at $z = 0.283$. The middle panel displays the image obtained with the narrowband filter and the right one the Hα emission after the continuum was subtracted. The putative host, and the galaxies G1 and G2 are at the same redshift as the GRB. Their projected distances are 7.3, 28.7 and 107.8 kpc, respectively (see also Tab. 7).

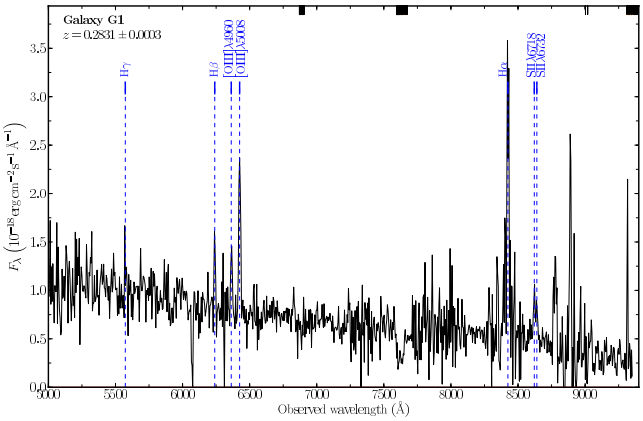

Figure 13. Spectrum of galaxy G1 (see Fig. 12 and Table 7). Several emission lines are detected at $z = 0.2831$. The $H\alpha$ emission line partly blended with a sky emission line. **Spectrum is not absolute flux-calibrated.**

the same redshift cannot be answered in this paper. Several GRB fields show an increased galaxy density, e.g. GRBs 000301C, 000926 (Fynbo et al. 2002), 011211 (Fynbo et al. 2003), 021004 and 030226 (Jakobsson et al. 2005), 030115 (Levan et al. 2006), and GRB 050820A (Chen 2012), however not the closest burst GRB 980425 (Foley et al. 2006). In addition, there are no comparison to field galaxies available, which makes it impossible to draw any firm conclusion.

The right panel in Fig. 12 shows the Hα image of the region of the GRB, including the host galaxy and the two closest galaxies with Hα emission at the same redshift. The explosion site is not particularly bright with respect to the nucleus of the host galaxy. Because the extinction in the nucleus and the explosion site are similar, this difference in brightness directly translates into a difference in the star-formation rate. Hence, the star-formation activity is not enhanced at the explosion site. Using a similar method to the one presented by

Table 7
Coordinates and distance to the afterglow of the galaxies with emission consistent with Hα at $z = 0.283$ detected in the GTC images

Galaxy	RA(J2000)	DEC (J2000)	Distance (kpc)
Host	09:07:38.51	+14:01:08.46	7.3
G1	09:07:39.43	+14:01:27.83	107.8
G2	09:07:38.87	+14:01:09.12	28.7
G3	09:07:42.86	+14:00:15.40	355.8

Fruchter et al. (2006), we find that the brightness of the region under the GRB corresponds to a percentile XXX.

Speculation: Low luminosity GRB/SNe, such as GRB 120422, seem not to follow the tendency of classical, cosmological GRBs of clustering in the brightest regions of the host, being in this sense more closely related to core-collapse SNe that are distributed in a more random way on the host.

After we have investigated the host environment, we will briefly summarise the properties of the galaxies at the same redshift. Figure 13 shows the spectrum of G1. The continuum is very blue typical for a galaxy that undergoes a starburst episode. We detect several strong emission lines at a common redshift of $z = 0.2831 \pm 0.0003$. The velocity difference between the GRB host galaxy and G1 is $119\,\mathrm{km\,s^{-1}}$.

Thomas: Could we fit the SED of G1-G3 with Le Phare? TBC: Andrew, Joe: What is your opinion?

4. DISCUSSIONS AND CONCLUSIONS

4.1. *The nature of GRB 120422A*

4.2. *The afterglow of GRB 120422A*

4.3. *SN 2012bz in the context of other GRB-SN*

4.4. *The host galaxy and galaxy environment*

Table 8
Log of optical and NIR observations

Phase (s)	error (s)	Instrument	Filter	Exposure time (s)	Brightness (mag)
664.2		*Swift*/UVOT	*uvw2*	38.9	> 20.27
1110.2		*Swift*/UVOT	*uvw2*	38.9	$20.30^{+0.55}_{-0.36}$
6244.8		*Swift*/UVOT	*uvw2*	332.2	$20.50^{+0.19}_{-0.16}$
2350484		*Swift*/UVOT	*uvw2*	16823.3	> 24.05
935.9		*Swift*/UVOT	*uvm2*	77.8	$20.84^{+0.75}_{-0.44}$
5967.3		*Swift*/UVOT	*uvm2*	196.6	$20.89^{+0.47}_{-0.33}$
11694.8		*Swift*/UVOT	*uvm2*	885.6	$21.03^{+0.23}_{-0.19}$
2347530		*Swift*/UVOT	*uvm2*	16365	> 23.73
912.7		*Swift*/UVOT	*uvw1*	58.3	> 20.56
5454.6		*Swift*/UVOT	*uvw1*	393.2	$21.43^{+0.48}_{-0.33}$
12479.4		*Swift*/UVOT	*uvw1*	645.3	$21.56^{+0.37}_{-0.28}$
25671.6		*Swift*/UVOT	*uvw1*	1771.2	$21.47^{+0.21}_{-0.18}$
2402743		*Swift*/UVOT	*uvw1*	11529.3	> 23.43
387.2		*Swift*/UVOT	*u*	245.8	$21.06^{+0.51}_{-0.35}$
898.9		*Swift*/UVOT	*u*	52.9	> 20.08
5659.9		*Swift*/UVOT	*u*	393.2	$21.08^{+0.43}_{-0.31}$
19853.4		*Swift*/UVOT	*u*	1770.3	$21.47^{+0.27}_{-0.21}$
29800.8		*Swift*/UVOT	*u*	651.6	$21.41^{+0.39}_{-0.29}$
242229.9		*Swift*/UVOT	*u*	11277.9	> 22.94
1096947		*Swift*/UVOT	*u*	69897.4	$23.00^{+0.17}_{-0.14}$
3258148		*Swift*/UVOT	*u*	27766.2	> 23.32
3328.3		*Swift*/UVOT	*b*	451.6	> 20.42
20641.6		*Swift*/UVOT	*b*	1523.7	$20.95^{+0.39}_{-0.28}$
116790.9		*Swift*/UVOT	*b*	1444	> 21.07
1914851		*Swift*/UVOT	*b*	7250.3	$21.54^{+0.36}_{-0.27}$
4665241		*Swift*/UVOT	*b*	449.7	> 19.82
90.4		*Swift*/UVOT	*v*	9	> 17.52
912.0		*Swift*/UVOT	*v*	77.7	> 18.83
20785.9		*Swift*/UVOT	*v*	1607.4	> 20.28
156431		*Swift*/UVOT	*v*	1282.9	> 20.27
4665526		*Swift*/UVOT	*v*	449.8	> 19.17
59563	345	GROND	g'	4×115	22.21 ± 0.10
61702	864	GROND	g'	4×369	22.12 ± 0.05
63556	861	GROND	g'	4×369	22.15 ± 0.07
63883	30	Gemini/GMOS	g'	$\times$	22.22 ± 0.06
65383	860	GROND	g'	4×369	22.11 ± 0.08
68118	1777	GROND	g'	8×369	22.18 ± 0.06
75361	450	P60	g'	$\times$	22.14 ± 0.10
152661	1534	GROND	g'	16×115	22.59 ± 0.10
155811	1516	GROND	g'	16×115	22.79 ± 0.16
340286	50	Gemini/GMOS	g'	$\times$	22.86 ± 0.06
753173	1776	GROND	g'	8×369	22.38 ± 0.10
925358	1775	GROND	g'	8×369	22.35 ± 0.08
1267371	50	GTC/Osiris	g'	$\times$	22.14 ± 0.11
1291574	15	Gemini/GMOS	g'	$\times$	22.16 ± 0.07
1702443	1772	GROND	g'	8×369	22.22 ± 0.04
1703734	60	Gemini/GMOS	g'	$\times$	22.19 ± 0.07
2474262	856	GROND	g'	4×369	22.82 ± 0.05
3362396	2242	GROND	g'	24×115	23.29 ± 0.20
9793	10	Gemini/GMOS	r'		21.11 ± 0.04
59563	345	GROND	r'	4×115	22.19 ± 0.14
61702	864	GROND	r'	4×369	22.17 ± 0.07
63556	861	GROND	r'	4×369	22.02 ± 0.05
64459	30	Gemini/GMOS	r'		22.10 ± 0.05
65383	860	GROND	r'	4×369	22.22 ± 0.07
68118	1777	GROND	r'	8×369	22.12 ± 0.08
74357	450	P60	r'		22.28 ± 0.10
137134	600	NOT/MOSCA	r'	4×300	22.28 ± 0.08
152661	1534	GROND	r'	16×115	22.34 ± 0.09
155811	1516	GROND	r'	16×115	22.47 ± 0.12
228856	1800	NOT/MOSCA	r'	12×300	22.23 ± 0.06
314237	1800	NOT/ALFOSC	r'	24×150	22.07 ± 0.06
340990	60	Gemini/GMOS	r'		22.12 ± 0.06
753173	1776	GROND	r'	8×369	21.48 ± 0.05
835203	600	NOT/StanCAM	R	8×150	21.45 ± 0.10
925358	1775	GROND	r'	8×369	21.33 ± 0.04
1179975	15	Gemini/GMOS	r'		21.41 ± 0.10
1260196	900	NOT/StanCAM	R	12×150	21.25 ± 0.06
1267581	50	GTC/Osiris	r'		21.37 ± 0.14
1292332	15	Gemini/GMOS	r'		21.26 ± 0.05
1520199	600	NOT/ALFOSC	r'	8×150	21.23 ± 0.07
1704797	60	Gemini/GMOS	r'		21.27 ± 0.05
1702443	1772	GROND	r'	8×369	21.21 ± 0.04
1957915	15	Gemini/GMOS	r'		21.32 ± 0.06
2126451	675	NOT/ALFOSC	r'	15×90	21.36 ± 0.08
2297894	720	NOT/MOSCA	r'	16×90	21.48 ± 0.05
2304100	50	Gemini/GMOS	r'		21.51 ± 0.04
2309230	270	Magellan/LDSS3	r'	3×180	21.55 ± 0.04
2474262	856	GROND	r'	4×369	21.65 ± 0.04
2475887	675	NOT/MOSCA	r'	15×90	21.54 ± 0.08
2477779	1250	DuPont/CCD	r'	4×500	21.58 ± 0.05
2649489	50	Gemini/GMOS	r'		21.73 ± 0.04
2643961	675	NOT/MOSCA	r'	15×90	21.79 ± 0.07
2735091	50	Gemini/GMOS	r'		21.77 ± 0.08
2817199	450	NOT/ALFOSC	r'	10×90	21.96 ± 0.07
3362396	2242	GROND	r'	24×115	22.43 ± 0.11
3512502	15	Gemini/GMOS	r'		22.41 ± 0.11
3854715	450	NOT/ALFOSC	r'	20×90	22.39 ± 0.47
1880	120	Gemini/GMOS	i'	$\times$	20.93 ± 0.04
51451	1800	NOT/MOSCA	I	12×300	22.19 ± 0.08
59563	345	GROND	i'	4×115	22.01 ± 0.18
61702	864	GROND	i'	4×369	22.13 ± 0.07
63556	861	GROND	i'	4×369	22.27 ± 0.10
64459	30	Gemini/GMOS	i'	$\times$	22.16 ± 0.06
67209	2686	GROND	i'	12×369	22.32 ± 0.09
73289	450	P60	i'	$\times$	22.23 ± 0.17
135683	600	NOT/MOSCA	i'	4×300	22.48 ± 0.12
152661	1534	GROND	i'	16×115	22.50 ± 0.16
155811	1516	GROND	i'	16×115	22.59 ± 0.19
226705	900	NOT/MOSCA	i'	6×300	22.37 ± 0.13
308045	10	GTC/Osiris	i'	$\times$	22.33 ± 0.14
309735	1950	NOT/ALFOSC	i'	13×300	22.35 ± 0.06
341689	50	Gemini/GMOS	i'	$\times$	22.29 ± 0.06
395133	900	NOT/ALFOSC	i'	12×150	22.18 ± 0.08
742159	1575	NOT/ALFOSC	i'	3150[a]	21.56 ± 0.08
753173	1776	GROND	i'	8×369	21.56 ± 0.08
836905	600	NOT/StanCam	i_i	8×150	21.52 ± 0.08
925358	1775	GROND	i'	8×369	21.49 ± 0.05
1262736	900	NOT/StanCAM	i_i	12×150	21.34 ± 0.05
1261613	10	GTC/Osiris	i'	$\times$	21.20 ± 0.09
1267805	50	GTC/Osiris	i'	$\times$	21.27 ± 0.06
1284132	900	P60	i'	$\times$	21.21 ± 0.14
1292809	15	Gemini/GMOS	i'	$\times$	21.29 ± 0.05
1371560	1800	P60	i'	$\times$	21.26 ± 0.11
1432840	600	NOT/StanCAM	i_i	8×150	21.35 ± 0.05
1692472	825	NOT/ALFOSC	i'	11×150	21.32 ± 0.07
1702443	1772	GROND	i'	8×369	21.27 ± 0.03
1702494	120	Gemini/GMOS	i'	$\times$	21.24 ± 0.04
1890072	1620	P60	i'	$\times$	21.22 ± 0.14
1976858	1800	P60	i'	$\times$	21.27 ± 0.15
2037796	900	NOT/ALFOSC	i'	15×90	21.46 ± 0.22
2063213	1800	P60	i'	$\times$	21.33 ± 0.10
2124602	600	NOT/ALFOSC	i'	10×120	21.41 ± 0.17
2300003	600	NOT/MOSCA	i'	10×120	21.29 ± 0.05
2310267	270	Magellan/LDSS3	i'	3×180	21.33 ± 0.04
2473900	600	NOT/MOSCA	i'	10×120	21.35 ± 0.05
2474262	856	GROND	i'	4×369	21.47 ± 0.06
2480838	1250	DuPont/CCD	i'	4×500	21.41 ± 0.04
2559358	570	NOT/MOSCA	i'	19×60	21.39 ± 0.06

Note. — Magnitudes are given in the AB photometric system and are corrected for Galactic extinction ($E(B-V) = 0.03$ mag). Column "Phase" shows the logarithmic mean-time after the GRB in the observer frame. We only display the total observing time of the *Swift*/UVOT data (see Sect. 2.1.1 for details). As described in Sect. 2.2, photometry was tied to SDSS DR8 in the optical ($u'g'r'i'z'$) and to 2MASS in the NIR (JHK_S). For those filters not covered by our primary calibration systems (i.e. R, I_C, i_i, or Y) we used the instrument-specific band passes to transform magnitudes into the respective filter system. **Exposures times of CAHA, Gemini, GTC and P60 data.**

Tab. 8 — continued

[a]The image is a stack of images with different exposure times. The shown time is the sum of the single images.

Phase (s)	error (s)	Instrument	Filter	Exposure time (s)	Brightness (mag)
2582542	360	P60	i'	×	21.50 ± 0.09
2655131	450	Magellan/LDSS3	i'	3×300	21.40 ± 0.06
2667689	1170	P60	i'	×	21.59 ± 0.15
2736187	60	Gemini/GMOS	i'	×	21.62 ± 0.04
2816120	585	NOT/ALFOSC	i'	13×90	21.63 ± 0.08
3248536	900	NOT/ALFOSC	i'	20×90	21.98 ± 0.09
3362396	2242	GROND	i'	24×115	22.06 ± 0.12
3507261	1350	NOT/ALFOSC	i'	30×90	22.08 ± 0.11
3852020	900	NOT/ALFOSC	i'	20×90	22.15 ± 0.21
59563	345	GROND	z'	4×115	22.01 ± 0.20
63541	2703	GROND	z'	12×369	22.09 ± 0.11
65605	30	Gemini/GMOS	z'	×	22.16 ± 0.11
68118	1777	GROND	z'	8×369	22.37 ± 0.17
152661	1534	GROND	z'	8×369	22.17 ± 0.16
155811	1516	GROND	z'	8×369	22.28 ± 0.27
342383	50	Gemini/GMOS	z'	×	22.59 ± 0.07
753173	1776	GROND	z'	8×369	21.86 ± 0.15
913895	900	CAHA	z'	×	21.93 ± 0.08
925358	1775	GROND	z'	8×369	21.78 ± 0.12
1119664	868	UKIRT/WFCAM	z'	4×360	21.44 ± 0.13
1268047	50	GTC/Osiris	z'	×	21.58 ± 0.07
1293429	15	Gemini/GMOS	z'	×	21.63 ± 0.06
1699722	60	Gemini/GMOS	z'	×	21.48 ± 0.04
1702443	1772	GROND	z'	8×369	21.48 ± 0.07
2471861	780	NOT/MOSCA	z'	12×120	21.74 ± 0.15
2474262	856	GROND	z'	4×369	21.62 ± 0.07
2557129	780	NOT/MOSCA	z'	13×120	21.59 ± 0.12
2736894	60	Gemini/GMOS	z'	×	21.86 ± 0.06
3362396	2242	GROND	z'	24×115	21.81 ± 0.12
917552	900	CAHA/Omega$_{2000}$	Y	×	21.93 ± 0.17
4589	180	UKIRT/WFCAM	J	360	20.20 ± 0.06
5048	180	UKIRT/WFCAM	J	360	20.33 ± 0.07
5514	180	UKIRT/WFCAM	J	360	20.36 ± 0.07
5979	180	UKIRT/WFCAM	J	360	20.41 ± 0.07
829616	1800	CAHA/Omega$_{2000}$	J	×	21.60 ± 0.17
922069	1800	CAHA/Omega$_{2000}$	J	×	21.83 ± 0.20
1117569	868	UKIRT/WFCAM	J	4×360	21.75 ± 0.24
1294514	270	Gemini-N/NIRI	J	×	21.96 ± 0.11
2244761	1339	UKIRT/WFCAM	J	6×360	21.90 ± 0.15
854426	1890	P200/WIRC	J	15×240	21.68 ± 0.16
6493	180	UKIRT/WFCAM	H	360	20.29 ± 0.09
6963	180	UKIRT/WFCAM	H	360	20.32 ± 0.09
7432	180	UKIRT/WFCAM	H	360	20.51 ± 0.11
7894	180	UKIRT/WFCAM	H	360	20.34 ± 0.10
92266	877	UKIRT/WFCAM	H	4×360	21.65 ± 0.42
262155	871	UKIRT/WFCAM	H	4×360	22.29 ± 0.31
1290555	282	Gemini-N/NIRI	K	???	21.46 ± 0.14

Tab. 8 — continued

SS acknowledges support by a Grant of Excellence from the Icelandic Research Fund, from the University of Iceland Research Fund, from the Dark Cosmology Centre, where part of this study was performed, and from the Iniciativa Cientifica Milenio grant P10-064-F (Millennium Center for Supernova Science), with input from "Fondo de Innovación para la Competitividad, del Ministerio de Economía, Fomento y Turismo de Chile", and Basal-CATA (PFB-06/2007). JPUF acknowledges support from the ERC-StG grant EGGS-278202.

The Dark Cosmology Centre is funded by the Danish National Research Foundation. Based on observations carried out with the IRAM Plateau de Bure Interferometer. IRAM is supported by INSU/CNRS (France), MPG (Germany) and IGN (Spain).

This work made use of data supplied by the UK *Swift*Science Data Centre at the University of Leicester.

Facilities: ESO/VLT (X-shooter), CAHA (BUSCA, CAFOS, Omega$_{2000}$), CARMA, Gemini (GMOS-S, GMOS-N, NIRI), GMG (???), GTC (OSIRIS), JCMT/SCUBA-2, Keck (LRIS), Magellan (LDSS3), NOT (ALFOSC, MOSCA, and StanCam), P60, PdBI, SMA, UKIRT (WFCAM), *XMM/Newton*

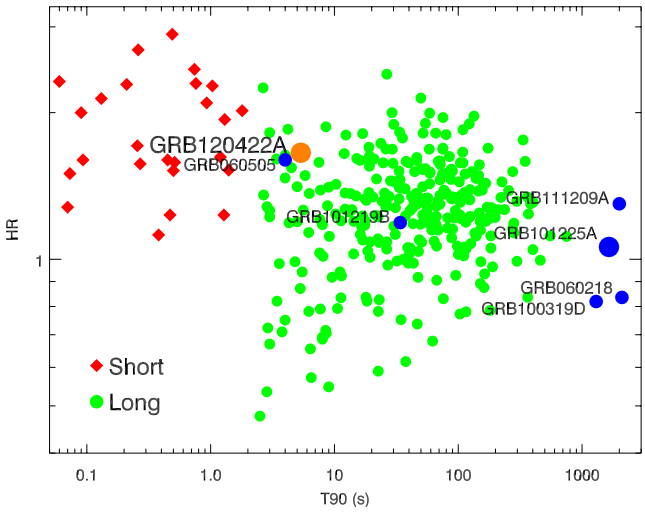

Figure 14. Hardness duration distribution of long and short GRBs (adapted from Kouveliotou et al. 1993). GRB 120422A populates a part of the parameters space that is typical for short-lasting long duration bursts with a hard spectrum, but distinct from the area where low-luminosity bursts ($T_{90} > 1000$ s,) are found. For comparison, the location of the short-lasting long-duration burst GRB 060505 is marked. For this burst no supernova down to very deep limits has not been detected. GRB 101219B is highlighted as an example of a typical long-duration GRB with spectroscopically-confirmed supernova. The circle size of the highlighted bursts indicates the redshift.

REFERENCES

Aihara, H., et al. 2011, ApJS, 193, 29
Arnett, W. D. 1982, ApJ, 253, 785
Arnouts, S., Cristiani, S., Moscardini, L., Matarrese, S., Lucchin, F., Fontana, A., & Giallongo, E. 1999, MNRAS, 310, 540
Barthelmy, S. D., et al. 2005, Space Sci. Rev., 120, 143
Berger, E., et al. 2011, ApJ, 743, 204
Bertin, E., & Arnouts, S. 1996, A&AS, 117, 393
Blinnikov, S. I., Eastman, R., Bartunov, O. S., Popolitov, V. A., & Woosley, S. E. 1998, ApJ, 496, 454
Bloom, J. S., Kulkarni, S. R., & Djorgovski, S. G. 2002, AJ, 123, 1111
Bromberg, O., Nakar, E., & Piran, T. 2011, ApJ, 739, L55
Bruzual, G., & Charlot, S. 2003, MNRAS, 344, 1000
Bufano, F., et al. 2012, ApJ, 753, 67
Burrows, D. N., et al. 2005, Space Sci. Rev., 120, 165
Calzetti, D., Armus, L., Bohlin, R. C., Kinney, A. L., Koornneef, J., & Storchi-Bergmann, T. 2000, ApJ, 533, 682
Campana, S., et al. 2006, Nature, 442, 1008
Cano, Z., et al. 2011, ApJ, 740, 41
Chabrier, G., Baraffe, I., Allard, F., & Hauschildt, P. 2000, ApJ, 542, 464
Chen, H.-W. 2012, MNRAS, 419, 3039
Chornock, R., et al. 2010, arXiv:1004.2262
Christensen, L., Fynbo, J. P. U., Prochaska, J. X., Thöne, C. C., de Ugarte Postigo, A., & Jakobsson, P. 2011, ApJ, 727, 73
Clocchiatti, A., Suntzeff, N. B., Covarrubias, R., & Candia, P. 2011, AJ, 141, 163
Cucchiara, A., Levan, A., Fox, D. B., & Tanvir, N. R. 2012, GCN Circ., 13245
De Cia, A., et al. 2011, MNRAS, 418, 129
de Ugarte Postigo, A., et al. 2012, A&A, 538, A44
Della Valle, M., et al. 2006a, Nature, 444, 1050
—. 2006b, ApJ, 642, L103
—. 2008, Central Bureau Electronic Telegrams, 1602
Ensman, L., & Burrows, A. 1992, ApJ, 393, 742
Evans, P. A., et al. 2007, A&A, 469, 379
—. 2009, MNRAS, 397, 1177
Ferrero, P., et al. 2006, A&A, 457, 857
Foley, S., Watson, D., Gorosabel, J., Fynbo, J. P. U., Sollerman, J., McGlynn, S., McBreen, B., & Hjorth, J. 2006, A&A, 447, 891

Fruchter, A. S., et al. 2006, Nature, 441, 463
Fynbo, J. P. U., et al. 2002, A&A, 388, 425
—. 2003, A&A, 406, L63
—. 2006, Nature, 444, 1047
—. 2010, MNRAS, 408, 2128
Fynbo, J. U., et al. 2000, ApJ, 542, L89
Gal-Yam, A., et al. 2006, Nature, 444, 1053
Galama, T. J., et al. 1998, Nature, 395, 670
Goad, M. R., et al. 2007, A&A, 476, 1401
Goldoni, P., Royer, F., François, P., Horrobin, M., Blanc, G., Vernet, J., Modigliani, A., & Larsen, J. 2006, in Society of Photo-Optical Instrumentation Engineers (SPIE) Conference Series, Vol. 6269, Society of Photo-Optical Instrumentation Engineers (SPIE) Conference Series
Greiner, J., et al. 2003, ApJ, 599, 1223
—. 2007, The Messenger, 130, 12
—. 2008, PASP, 120, 405
Hamuy, M., & Pinto, P. A. 2002, ApJ, 566, L63
Hjorth, J., & Bloom, J. S. 2011, arXiv:1104.2274
Hjorth, J., et al. 2003, Nature, 423, 847
Hook, I. M., Jørgensen, I., Allington-Smith, J. R., Davies, R. L., Metcalfe, N., Murowinski, R. G., & Crampton, D. 2004, PASP, 116, 425
Ilbert, O., et al. 2006, A&A, 457, 841
Jakobsson, P., et al. 2005, MNRAS, 362, 245
Kalberla, P. M. W., Burton, W. B., Hartmann, D., Arnal, E. M., Bajaja, E., Morras, R., & Pöppel, W. G. L. 2005, A&A, 440, 775
Kann, D. A., et al. 2011, ApJ, 734, 96
Kouveliotou, C., Meegan, C. A., Fishman, G. J., Bhat, N. P., Briggs, M. S., Koshut, T. M., Paciesas, W. S., & Pendleton, G. N. 1993, ApJ, 413, L101
Kron, R. G. 1980, ApJS, 43, 305
Krühler, T., et al. 2008, ApJ, 685, 376
—. 2011a, A&A, 526, A153
—. 2011b, A&A, 534, A108
Larson, D., et al. 2011, ApJS, 192, 16
Levan, A., et al. 2006, ApJ, 647, 471
Maeda, K., Mazzali, P. A., Deng, J., Nomoto, K., Yoshii, Y., Tomita, H., & Kobayashi, Y. 2003, ApJ, 593, 931
Malesani, D., et al. 2004, ApJ, 609, L5
—. 2012a, GCN Circ., 13275
—. 2012b, GCN Circ., 13277
Martin, S., Petitpas, G., & de Ugarte Postigo, A. 2012, GCN Circ., 13260
Matheson, T., et al. 2003, ApJ, 599, 394
Melandri, A., et al. 2012, A&A, 547, A82
Modjaz, M., et al. 2009, ApJ, 702, 226
Monet, D. G., et al. 2003, AJ, 125, 984
Nardini, M., Schmidl, S., Greiner, J., & Kann, D. A. 2012, GCN Circ., 13256
Ofek, E. O., et al. 2007, ApJ, 662, 1129
Oke, J. B., et al. 1995, PASP, 107, 375
Olivares E., F., et al. 2012, A&A, 539, A76
Patat, F., et al. 2001, ApJ, 555, 900
Perley, D. A. 2012, GCN Circ., 13278
Perley, D. A., Cucchiara, A., Cenko, S. B., Levan, A. J., Kulkarni, S. R., Ben-Ami, S., & Cao, Y. 2012a, GCN Circ., 13267
Perley, D. A., Jones, T., & Ellis, R. 2012b, GCN Circ., 13279
Phillips, M. M. 1993, ApJ, 413, L105
Pian, E., et al. 2006, Nature, 442, 1011
Piranomonte, S., et al. 2008, A&A, 492, 775
Poole, T. S., et al. 2008, MNRAS, 383, 627
Richardson, D., Branch, D., & Baron, E. 2006, AJ, 131, 2233
Roming, P. W. A., et al. 2005, Space Sci. Rev., 120, 95
Sánchez-Ramírez, R., et al. 2012, GCN Circ., 13281
Sault, R. J., Teuben, P. J., & Wright, M. C. H. 1995, in Astronomical Society of the Pacific Conference Series, Vol. 77, Astronomical Data Analysis Software and Systems IV, ed. R. A. Shaw, H. E. Payne, & J. J. E. Hayes, 433
Savaglio, S., Glazebrook, K., & Le Borgne, D. 2009, ApJ, 691, 182
Schulze, S., et al. 2012a, GCN Circ., 13257
—. 2012b, GCN Circ., 13257
Skrutskie, M. F., et al. 2006, AJ, 131, 1163
Smith, I. A., Tilanus, R. P. J., Tanvir, N. R., & Frail, D. A. 2012, GCN Circ., 13259
Soderberg, A. M., et al. 2012, ApJ, 752, 78
Sparre, M., et al. 2011, ApJ, 735, L24
Stanek, K. Z., et al. 2003, ApJ, 591, L17
Starling, R. L. C., Page, K. L., Pe'er, A., Beardmore, A. P., & Osborne, J. P. 2012, MNRAS, accepted, arXiv:1207.1444
Stritzinger, M., et al. 2002, AJ, 124, 2100
Tanvir, N. R., Levan, A. J., Cucchiara, A., & Fox, D. B. 2012, GCN Circ., 13251
Thöne, C. C., et al. 2008, ApJ, 676, 1151
—. 2011, Nature, 480, 72
Tinney, C., et al. 1998, IAU Circ., 6896, 3
Tody, D. 1993, in Astronomical Society of the Pacific Conference Series, Vol. 52, Astronomical Data Analysis Software and Systems II, ed. R. J. Hanisch, R. J. V. Brissenden, & J. Barnes, 173
Troja, E., et al. 2012, GCN Circ., 13243
Valenti, S., et al. 2008, MNRAS, 383, 1485
—. 2011, MNRAS, 416, 3138
Wiersema, K., et al. 2012, GCN Circ., 13276
Woosley, S. E., & Bloom, J. S. 2006, ARA&A, 44, 507
Yoldaş, A. K., Krühler, T., Greiner, J., Yoldaş, A., Clemens, C., Szokoly, G., Primak, N., & Klose, S. 2008, in American Institute of Physics Conference Series, Vol. 1000, American Institute of Physics Conference Series, ed. M. Galassi, D. Palmer, & E. Fenimore, 227
Zauderer, A., Berger, E., & Laskar, T. 2012, GCN Circ., 13254
Zeh, A., Klose, S., & Hartmann, D. H. 2004, ApJ, 609, 952
Zhang, B.-B., et al. 2012, ApJ, 756, 190